

Appendix A: Supplementary Information

Dual-Functional Nanofiltration and Adsorptive Membranes for PFAS and Organics Separation from Water

Francisco Léniz-Pizarro¹, Ronald J. Vogler¹, Phillip Sandman¹, Natalie Harris¹, Lindell E. Ormsbee², Chunqing Liu³, Dibakar Bhattacharyya^{1,*}

¹Department of Chemical and Materials Engineering, University of Kentucky, Lexington, KY 40506, USA

²Department of Civil Engineering, University of Kentucky, Lexington, KY 40506, USA

³Membranes R&D Group, Honeywell UOP, 50 E. Algonquin Road, Des Plaines, IL 60016, USA

* Corresponding author: Dibakar Bhattacharyya

University Alumni Chair Professor

Chemical and Materials Engineering, 177 FPAT Bldg

University of Kentucky, Lexington, KY 40506

Phone: 859-312-7790; email: db@uky.edu

1. Analytical and Experimental Details

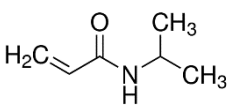
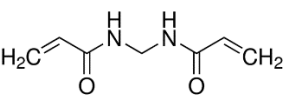
1.1. Materials and Chemicals details

Table S1. Chemical and materials used in experimental methods.

Item	Purity	Manufacturer	pKa (if applies)
Sodium Perfluorooctanoate	97%	Alfa Aesar	-
PFOA	95%	Alfa Aesar	[-0.5, 3.8] [1–6]
Potassium perfluorooctanesulfonate (PFOS)	98%	Matrix Scientific	[0.14, 1] [5–8]
Undecafluoro-2-methyl-3-oxahexanoic acid (GenX)	97%	Matrix Scientific	[-0.77, 2.8] [8–10]
Heptafluorobutyric acid (PFBA)	98%	Sigma-Aldrich	[0.08, 1.6] [5,7,11,12]
Sodium octanoate	>99.0%	TCI	-
Octanoic acid (caprylic acid)	>99.5%	MP	4.894 [13]
Pentanoic acid (valeric acid)	99%	ACROS ORGANICS	4.842 [13]
Propionic acid	>99%	J.T. Baker (Radnor, PA)	4.874 [13]
2,4,6 trichlorophenol (2,4,6 TCP)	98%	ACROS ORGANICS	6.10 [14]
Oxalic acid dihydrate	>99%	Sigma-aldrich	1.271, 4.266 [13]
L-Glutamic acid	>99.0%	TCI	2.162, 4.288, 9.387 [13]
Methylene blue chloride trihydrate	Reagent grade	VWR	
D-(+)-Xylose	>99%	Sigma-Aldrich	-
Sucrose	ACS grade	Fisher Scientific	-
Ethanol	Absolute	Millipore Sigma (Billerica, MA)	-
Sodium chloride	ACS grade	VWR (Solon, OH)	-
Sodium sulfate	99.7%	Fisher Scientific	-
Calcium chloride	ACS grade	BDH (Radnor, PA)	-
Hydrochloric acid	1 N Reagent grade	VWR	-
Sodium hydroxide	-	VWR Chemicals BDH	-
NF270	Nanofiltration membrane	Dow Filmtec	

Synthesis

Table S2. Chemical, materials, and solvents used for the chemical synthesis of polyaromatic amide layer and the pore-functionalization of the open structure material

Item	Purity	Manufacturer
Piperizine (PIP) anhydrous	99%	Spectrum (Gardena, CA)
Trimesoyl chloride (TMC) - 1,3,5-Benzenetricarbonyl chloride	98%	Millipore Sigma (Darmstadt, Germany)
N-isopropylacrylamide (NIPAm) 	98%	TCI
N-N-methylenebisacrylamide (MBA) 	>99%	Alfa Aesar (Ward hill, MA)
Ammonium persulfate (AMPS)	98%	ACROS ORGANICS (New Jersey, USA)
Water	ASTM type I	RICCA Chemical (Arlington, TX)
ISOPAR-G	Technical grade	Univar (Downers Grove, IL)
PVDF400	Porous membrane	Nanostone Sepro

1.2. Synthesis of a Thin Polyaromatic Amide Layer on Top of an Open Polymeric Structure

Impact of polymerization solution composition on functionalization:

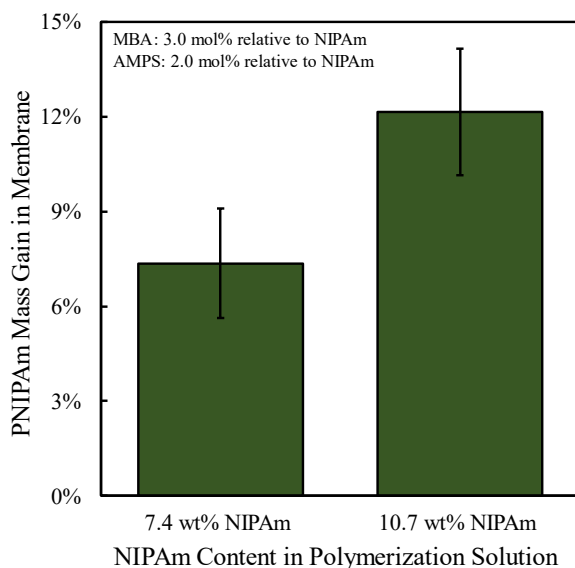


Figure S1. Mass gain of PNIPAm in PVDF 400 membranes as a function of the weight percentage of NIPAm in the polymerization solution. The concentrations of crosslinker and initiator were 3.0 mol% and 2.0 mol% relative to the molar amount of NIPAm. Each bar represents three samples.

1.3. Analytical and material characterization techniques details

1.3.1. LC-MSMS

A Shimadzu chromatograph model LC-20 AD and a SCIEX Flash Quant mass spectrometer (MS/MS) model 4000 Q Trap with electrospray ionization (ESI) was used. Isotopic mass labeled perfluoro-n-[1,2,3,4- $^{13}\text{C}_4$] heptanoic acid was used as internal standard at a concentration of 20 ppb. Samples were prepared in a 20 mM ammonium acetate solution in ASTM type 1 water. The mobile phases used were (1) 20 mM ammonium acetate and (2) methanol. Injection volume was 5 μL and a total flow of 0.4 mL/min with a gradient elution of the mobile phases (1) and (2). A Macherey Nagel analytical column EC 125/2 NUCLEODUR C18 Gravity packed with 5 μm particles, and length 125 x 2 mm ID. Calibration curve 1-150 ppb was created including initial blank sample. PFAS standards were obtained from Wellington laboratories. Quality controls

samples included negative controls, blank samples, calibration curve verification and half dilution samples. Limit of quantification (10 x background concentration) was in the range of 1-2 ppb for all PFAS tested.

1.3.2. ICP-MS

An inductively coupled plasma mass spectrometer from Agilent 7800 was used. Samples were prepared with 2% nitric acid solution. Plasma was used in general matrix mode. Calibration curve with a ~2,000x range (10-20,000 ppb) were made with a R=1.000. Scandium was used as reference internal standard. Quality control samples included negative controls, calibration curve verification and half dilutions. The Na⁺ detection limit was around 0.4 ppb and background equivalent concentration 8.5 ppb. For Cl⁻ the limit of detection was 14 ppb, but with a BEC of 300 ppb. For the case of Cl⁻ analysis, all solutions used contained 1% nitric acid instead of 2%. Chloride and sodium analytical standards used were obtained from ARISTAR VWR.

1.3.3. UV-Vis:

The detection limit of the 2,4,6 TCP was ~500 ppb, and the limit of quantification was around 2 ppm (or 0.01 mM).

1.3.4. Conductivity

Conductivity values were automatically corrected for 25°C (reported values). The limit of detection was ~1 uS/cm, and limit of quantification ~ 5 uS/cm equivalent to 400 ppb NaCl.

1.3.5. TOC

The limit of detection was ~ 600 ppb of total organic carbon, and the limit of quantification was around 5 ppm.

1.3.1. FESEM

The surface of the polymeric materials was observed under an electron microscope (FEI Helios Nanolab 660). Beam deceleration and immersion mode were used, and images were captured at 10,000 and 50,000x magnification. Surfaces were rinsed in DI water and dried in a convective oven at 30 °C before analyzing and no metal sputtering was applied to them.

1.3.1. XPS

A K-Alpha X-ray Photoelectron Spectrometer (XPS) from Thermo Scientific was used for analyzing the depth profile of the thin film composites. X-ray size of 400 μm and two different areas were analyzed per membrane for calculating the average and standard deviation of the elemental composition (%). Flood gun was used to reduce polymeric surface charge. For etching down into the polymeric material depth an argon ion beam was used, with ion energy of 1000 eV and current was set at Mid from instrument options. Cycle times and number of cycles depended on the experiment performed (fluorine detection or synthesis validation).

1.4. Membrane performance testing

1.4.1. Crossflow

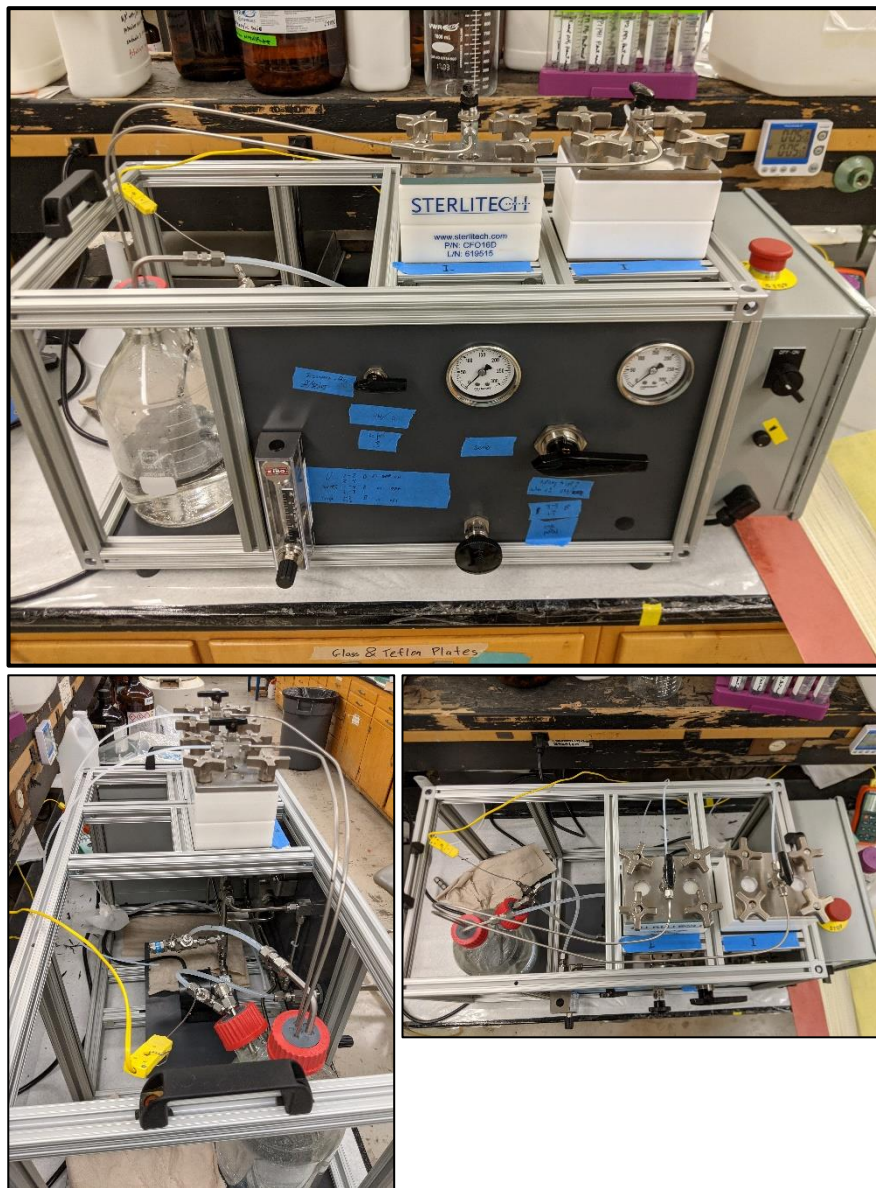


Figure S2. Small cross flow membrane testing unit for low generation of waste from tested solutions with contaminants, created in the Chemical and Materials Engineering department at the University of Kentucky.

1.4.2. Solute permeance analysis under diffusive flow:

The diffusive transport of PFOA, GenX, and PFBA - and Na₂SO₄ as a control - were quantified using an automated diffusion cell system from PermeGear (ILC07). A diagram of the instrument and details of the operation can be found elsewhere [15]. 7 cells were filled up simultaneously with 860 μL of solution containing 10 ppm of each one of the PFAS tested, and in a separate run, 750 ppm for sodium sulfate. A peristaltic pump kept a constant flow of ASTM type I water at a speed of 25 μL/min, maintaining the driving force from the permeate (collector) side. Four sequential samples were collected per diffusion cell over time, with 3 hours collection time per sample, meaning that the samples were collected at time 3, 6, 9, 12 hours.

The concentrations of the collected samples were measured and, in order to correlate to the solute permeance properties of the membrane, a solution-diffusion model was adopted ($J_{solute} = B \cdot \Delta C$). This assumes that the membranes tested behave as a reverse osmosis – denser membrane – and the transport of solutes is mediated in a more simplified fashion: solubility into the polymer and diffusion through the thin film, instead of including charge and other interactions (as presented in Eq. 1 and Eq. 2 in the body of the manuscript). The solute permeability coefficient (B) was calculated from the diffusive flux obtained for each solute, and the parameter used (initial feed concentration, pump speed or flow of pure water, membrane area, collection times).

2. Membrane characteristics

Table S3. Characteristics of membranes used in this work

	Commercial NF270 [16–20]	PIP/PAH-PS35 [21]	Commercial PVDF400
Isoelectric point pH (-)	~3.6	7	-
Modeled or visible pore radius (nm)	0.43*	0.44*	~50
Water contact angle (°)	56	72	80
Operating pH range	3-10 (and 1-12 for short times)	Stable at ~2.5	<12
Manufacturer	Dupont FilmTec	Our previous work (in lab) [21]	Nanostone Sepro

*Pore sizes were obtained from hindered transport model using neutral organic compounds. Values from literature.

3. Discussing PFAS Separation Using NF Membranes and Organic Anions

3.1. Towards a Zero Waste Discharge Alternative

To provide a long-term solution for separating PFAS out from water sources, a less hazardous, less complex, and more easily to handle mixture of PFAS also needs to be achieved. As previously explained, the separation mechanism of NF membranes is exclusion, and its separation yields remain mostly constant regardless of the solution concentration that needs to be treated. Figure S3 shows how this principle can be applied for a single step process in which a solution at ppm levels was concentrated down to 15% of the initial volume, thus increasing the PFOA concentration beyond 5 times. This is consistent to a pilot water treatment plant recently installed in Uppsala, Sweden. For their initial ppt level raw water they obtained 3.5 times more concentrated downstream operating in between 70-80% water recovery [22]. By applying high water recoveries and a few concentrating steps a small volume and highly concentrated PFAS stream can be obtained. This small volume becomes easier to handle and can be further combined with technologies for “destructing” PFAS in which fluorine is fully mineralized for a close-loop PFAS treatment.

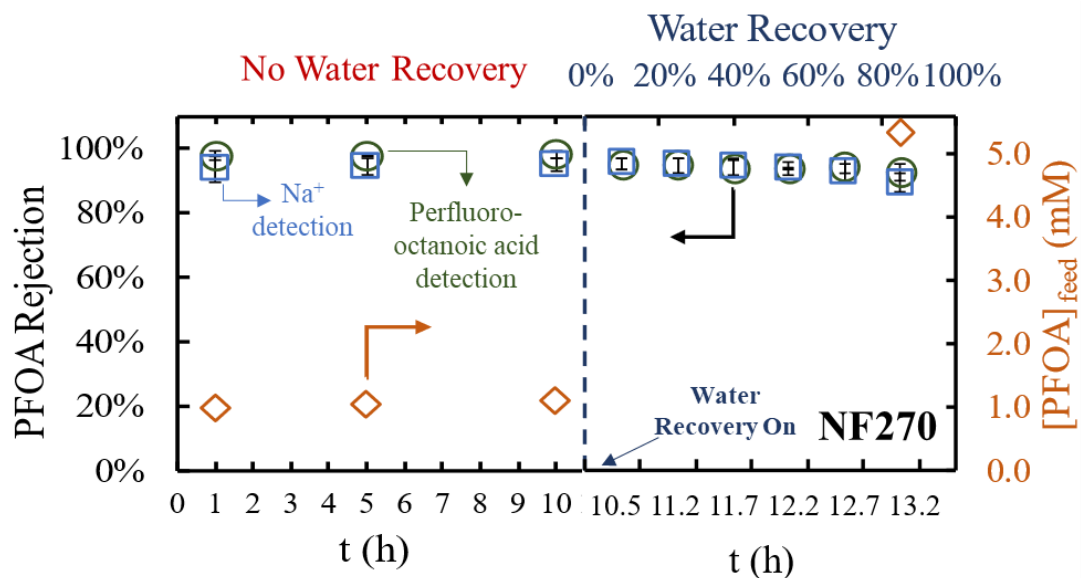


Figure S3. Separation stability in a long-run and water recovery mode for PFOA using commercial Dow NF270 membranes. Both the counterion (Na^+) and the PFOA concentrations were measured. A crossflow equipped with 2 cells was used, 436 ppm feed concentration of Sodium perfluoro octanoate, $T=27^\circ\text{C}$, flow rate of 3.5 (GPH), permeate flux= $68\text{ L}/(\text{m}^2\text{h})$ ($P=66\text{ psi}$), $\text{pH}\sim 8$

3.2. Octanoic acid separation at different pH range and initial counterion

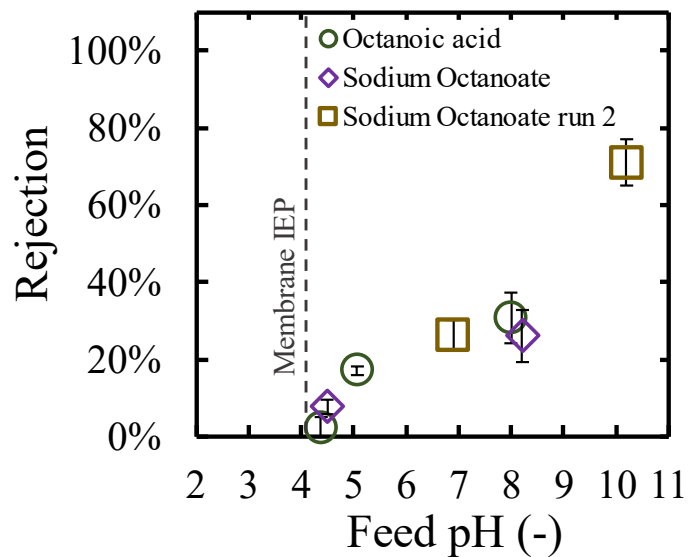


Figure S4. Effect of sodium as counterion and on electrolyte solution. Separation performance comparison between acid and sodium form of octanoate. 1 mM was initially fed. pH was adjusted using NaOH 0.1 mM. A cross-flow membrane system unit was used, with 2 membranes tested simultaneously, $T \sim 26^\circ\text{C}$, $J_w = 85 \pm 5$ (LMH). Octanoate was measured through total organic carbon (TOC), and sodium was measured through ICP-MS. Samples were taken after compaction with water and 3 hours of stabilization per measurement.

3.3. Control run of the NF membrane separation vs pH separating a neutral organic compound

Steady rejection and permeate flux of the neutral organic compounds xylose as a function of the aqueous solution pH, for both negatively charged NF membrane (commercial NF270) and synthesized more positively charged NF membrane PIP/PAH-PS35 [21] membrane.

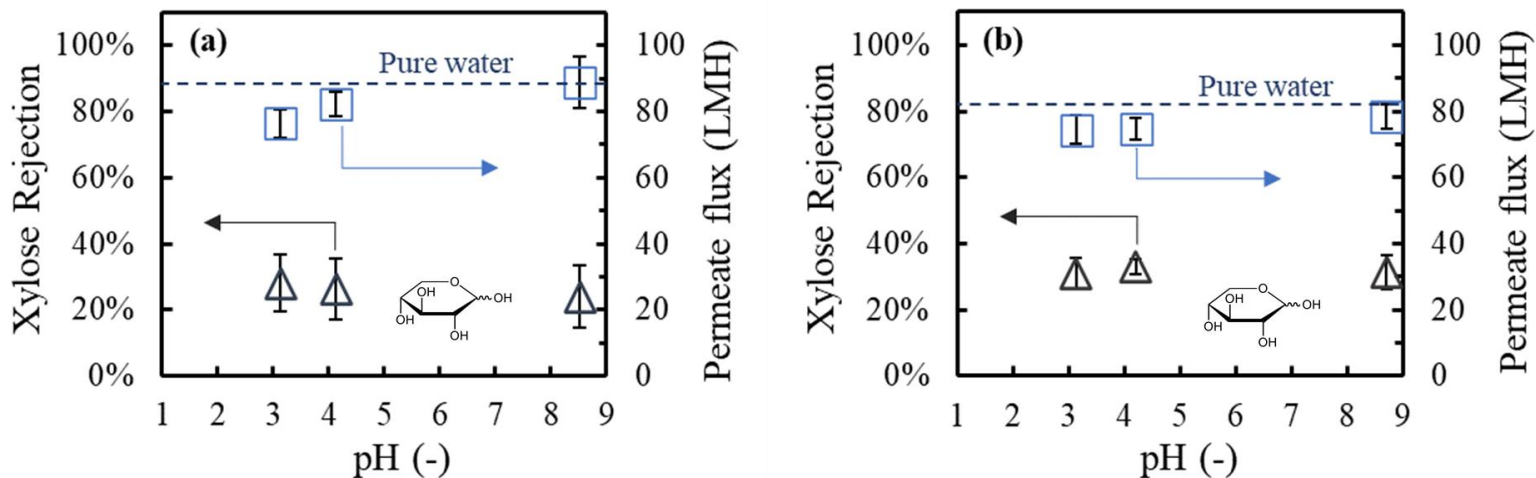


Figure S5. Water flux and rejection of neutral organic compound (Xylose) stability. NF membranes (a) commercial NF270 and (b) PIP/PAH. A crossflow membrane unit was used, with a feed aqueous solution consisting of 1 mM xylose. The operating conditions were: $T=26^{\circ}\text{C}$, $P=6.8$ bar (NF270) and 4.4 bar (PIP/PAH) keeping permeate flux similar. pH was variable as shown in plots. Pure water flux represented by a dotted line was calculated from the average of the pure water run previous and after the xylose solution. Xylose concentrations were measured using a total organic carbon (TOC).

3.4. Ionizable compounds/ions size and shape

Geometries in PFOA and octanoate: tetrahedral in the hydrophobic domain and trigonal planar on the carboxyl group. C, F, H properties presented in Table S4 [23].

Table S4. H, F and C properties

Van der Waals radii (Å)	H (1.2)	F (1.47)	C (1.70)	
Bond lengths (Å)	C-H (1.09)	C-F (1.35)	C-C (1.54)	C-O (1.43)
Electronegativities (Pauling scale)	H (2.1)	F (4.0)	C (2.5)	

Calculation of the critical chemical structure distance for the main ionizable compounds studied on the body of the manuscript

Length:

***Some bond angles were obtained using Avogadro Software. Triangle's calculations were helped using <https://www.mathwarehouse.com/triangle-calculator/online.php>.*

1) PFOA:

- Max (no angle): $7 * (C - C)_{length} + (C - O) = 7 * 1.54(\text{Å}) + 1.43(\text{Å}) = \mathbf{12.21(\text{Å})}$



Diagram for calculating the length of the compounds (reference example: PFOA). Red lines represent the 3 distances between the C-C-C angle.

- Min (112.5° on the C-C-C angle, and 120° on the C-C-O angle): $3 * 2.56(\text{Å}) + 2.57(\text{Å}) + 0.45(\text{Å}) = \mathbf{10.7(\text{Å})}$

2) Octanoate:

- Min: (111° on the C-C-C angle, and 118.3° on the C-C-O angle): $3 * 2.54(\text{Å}) + 2.55(\text{Å}) + 0.36(\text{Å}) = \mathbf{10.53(\text{Å})}$

3) Pentanoate:

- Min: (111° on the C-C-C angle, and 118.3° on the C-C-O angle): $2 * 2.54(\text{Å}) + \frac{1}{2} * 2.55(\text{Å}) + 0.36(\text{Å}) = \mathbf{6.72(\text{Å})}$

4) Propanoate:

- Min: (111° on the C-C-C angle, and 118.3° on the C-C-O angle): $1 * 2.54(\text{Å}) + \frac{1}{2} * 2.55(\text{Å}) + 0.36(\text{Å}) = \mathbf{4.18(\text{Å})}$

5) PFOS:

- Min: (112.5° on the C-C-C angle, and 120.3° on the C-S-O angle): $3 * 2.56(\text{Å}) + 2.90(\text{Å}) + 0.45(\text{Å}) = \mathbf{11.03(\text{Å})}$

Widest radial (shortest axis) distance:

To assess the radial distance of the PFOA (and octanoate) the tetrahedral geometry of the backbone was used. The base of the tetrahedral formed in between 3 atoms can be approximated to a circumscribed circle, and its radius will be considered as the radial distance of the compound modeled as a cylinder. Of course, as bonds can rotate to the axial axis, it would behave as a dynamic shape, however the areal circumference should remain. The widest section should be encountered where the largest bonds and atoms are found.

For the case of PFOA and PFOS:

C-F-F basal section. Angles used: F-C-F: 108.55°, F-C-C: 108.85°

For the case of the fatty acids:

C-H-H basal section. Angles used: H-C-H: 109.34°, H-C-C: 108.94°

For the calculation of the radius of the circumference, triangles were drawn in between the F-C-F, and the F-C-C, to obtain the distances shown in blue and brown on the triangles (Figure S6). Bond lengths were used from Table S4.

By triangles properties (angles and lengths) from Table S4 and Figure S6, the blue and brown segments of the triangles were found

For PFOA and PFOS:

- Brown segment: 2.19 (Å)
- Blue segments: 2.35 (Å)

For Fatty acids:

- Brown segment: 1.78 (Å)
- Blue segments: 2.16 (Å)

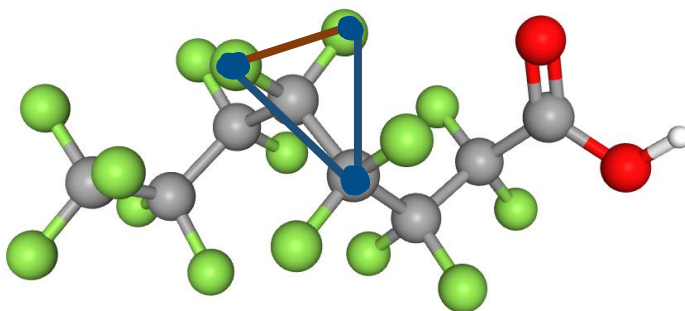


Figure S6. PFOA molecule and drawn triangle for circumscribed circle.

The radius of the circumference is going to be dictated by:

$$R = \frac{a^2}{\sqrt{4a^2 - b^2}} = \frac{2.35^2}{\sqrt{4 * 2.35^2 - 2.19^2}} \quad \text{Eq. S1}$$

Where a: equal side of triangle (blue), b base side (brown).

$$R_{PFOA} = 1.328 \text{ (Å)}$$

Similarly for fatty acid. Finally obtaining the diameters:

$$D_{PFOA} = 2.66 \text{ (\AA)}$$

$$D_{fatty\ acid} = 2.37 \text{ (\AA)}$$

And for the total circumference accounting for the atoms around this circumference (F, H and C, as it corresponds), 1 average diameter from their Van der Waals dimension of the 3 atoms was added to the total diameter of this radial distance:

$$D_{PFOA,total} = 2.66 + 3.1 = 5.76 \text{ (\AA)}$$

$$D_{fatty\ acid,total} = 2.66 + 2.73 = 5.39 \text{ (\AA)}$$

For the calculation of 2,4,6 TCP the diagonals end to end Cl – C (narrowest) and Cl – OH (widest) were calculated. For the chloride ion its crystal (non-hydrated) and hydrated values are shown from literature.

Table S5. Spatial dimensions for the ionizable compounds/ions used in the body of the manuscript.

Compound/ion	Radial diameter (nm)	Length (nm)
Propanoate	0.539	0.418
Pentanoate	0.539	0.672
Octanoate	0.539	1.053
PFOA	0.576	1.07
PFOS	0.576	1.103
2,4,6 TCP	Narrowest: 0.552* Widest: 0.671*	-
Chloride	Crystal (bare ionic): 0.362 [24,25] Hydrated: 0.664 [25]	-

*Calculations helped by Avogadro Software for obtaining angles and bond lengths.

3.5. Diffusion calculations for its use into the DSPM-DE

Diffusivity at infinity dilution ($D_{i,\infty}$):

Calculations were done using Wilke and Chang equation [26] Eq. S2. V_i is the solute molal volume at boiling point, which is calculated from group of contributions [27]. x is an association factor of the solvent obtained from [28] with a value of 2.26. M is the molecular weight of the solvent (18 g/mol). $T=25$ °C (298 K) was used in the experiments and therefore is used in this calculation, including the value of viscosity (0.0091 poise).

$$D_{i,\infty} = 7.4 \cdot 10^{-8} \frac{(xM)^{\frac{1}{2}} T}{\mu V_i^{0.6}} \quad \text{Eq. S2}$$

Calculation of molar volume at boiling point [27] :

$$V = 0.32 * L(L - 1) + \sum A_j * G_j \quad \text{Eq. S3}$$

- Propanoate: $V = 0.32 * 3 * (3 - 1) * [(27.38 * 1) + (19.02 * 1) + (37.71 * 1)] = 86.03 \left(\frac{cm^3}{mol}\right)$
- Pentanoate: $V = 128.55 \left(\frac{cm^3}{mol}\right)$
- Octanoate: $V = 197.13 \left(\frac{cm^3}{mol}\right)$
- PFOA: $V = 276.44 \left(\frac{cm^3}{mol}\right)$
- PFOS: $V = 291 \left(\frac{cm^3}{mol}\right)$
- 2,4,6 TCP: $V = 152.9 \left(\frac{cm^3}{mol}\right)$

Table S6. Diffusivity at infinity dilution for solutes studied in water

Molecule/ion	$D_{i,\infty}$ (m^2/s) $\cdot 10^{-9}$ at 25°C
Propanoate	1.07
Pentanoate	0.84
Octanoate	0.65
PFOA	0.53*
PFOS	0.514*
2,4,6 TCP	0.756
Cl ⁻	2.03** [21]

* Values comparable to the ones calculated by L. Pereira et. al. [29] through computer simulation.

**Calculated using the limiting molar (equivalent) ionic conductivity

3.6. Other partitioning effects: charge and adsorption

To evaluate the contribution of the surface charge to the partitioning of PFOA a more positively charged NF membrane was compared to the negatively charged NF270. PIP/PAH-PS35 [21] has an IEP ~ pH 7 and modeled pore radius around 0.44 nm, similar to the NF270 (rp~0.43 nm). Figure S5 shows the results of the separation of neutral xylose for both membranes, as a control, proving similar and independent-of-pH values. The separation of PFOA using the PIP/PAH-PS35 is presented in Figure S7. Results were around 20% lower in magnitude compared to NF270 results (Figure S3). This decrease was further investigated using an X-ray photoelectron spectrometer (XPS). Post PFOA separation membranes were rinsed, and water was run through them for at least 3 hours. Adsorbed PFOA was detected by the fluorine content on the membrane depth profile using XPS (Figure S8). NF270 had detectable fluorine in the first top 10 nm, however background levels were reached after the first etch. Density functional theory calculation of the Gibbs free energies of a few PFAS-membrane were reported by M. Li, et. al. [30], and negative values suggested potential adsorption into the membrane. On the other hand, the more positively charged membrane presented twice as much fluorine in the top 10 nm, and consistent detectable levels over the depth profile. This suggests that NF membranes which contain an increased number of amine groups in the surface will partition more PFOA and consequently decrease its rejection performance.

To evaluate if the charge repulsion of the strong electrolyte PFOA can explain its high separation rates, model multivalent organic anions oxalate and glutamic acid, and the inorganic anion sulfate were tested using the NF270 membranes (Figure S9). Even though all three ions achieve rejections close to 90% at pH~7, the differences between their slopes from the rejection vs pH graphs provided supplemental information. Sulfate acts as a reference ion since pH does not affect the

magnitude of the charge of SO_4^{2-} . Oxalate had a steeper slope than sulfate corresponding to the simultaneous decrease in charge magnitude of the solute and the surface, with rejections as low as 30% at pH 3. The slope observed in glutamate was like the one for sulfate when $\text{pH} > \text{IEP}$, however the rejection was stabilized at the membrane IEP with values around 65% while sulfate kept falling. The fact that oxalate and sulfate with rejections $>90\%$ dropped to $<50\%$ at pH values below the membrane IEP, and that octanoate reached near 0% rejection even before the IEP, while the rejection of the strong electrolyte PFOA remains as high as 90% (comparable to other results using NF270 around its IEP from literature: 87% and 75% [15,31]), supports a hypothesis that the Donnan exclusion alone cannot explain the high PFOA rejections at low pH.

To correlate the partitioning of organic compounds from water into the polymeric NF layer, the octanol-water partitioning coefficients (K_{ow}) of the FAs and PFAS (Table S7) were studied, and Eq. S3 was used to observe the effect of ionization. Results were plotted in Figure S10.

Hydration effects were not studied because these were assumed to be negligible. This assumption is supported by the fact that fluorine is a poor electron donor [23] and that hydration on the hydrophilic carboxylic acid will be comparable to the one from octanoate

3.6.1. Positively charged membrane separation of PFOA (long term and water recovery)

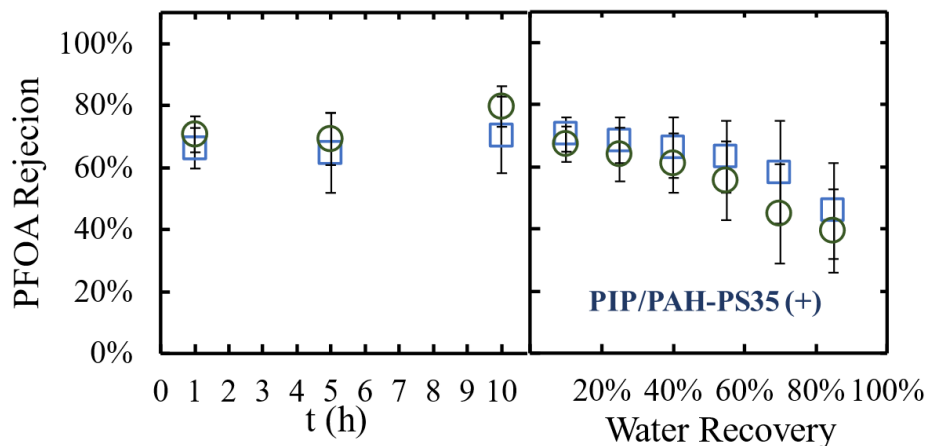


Figure S7. Long-run and water recovery mode separation of PFOA using a lab-synthesized piperazine-polyallylamine-trimesoychloride positively charged NF membrane on top of a commercial UF PS35 membrane from Solecta membranes. Both the counterion (Na^+) and the PFOA concentrations were measured. A crossflow equipped with 2 cells were used, 1 mM feed concentration of Sodium perfluoro octanoate, $T=27\text{ C}$, $\text{GPH}=3.5$, $J_w=68\pm 2$ ($P=66\text{ psi}$). $\text{pH}=7.18$

3.6.2. *PFOA adsorption due to charge (amine groups)*

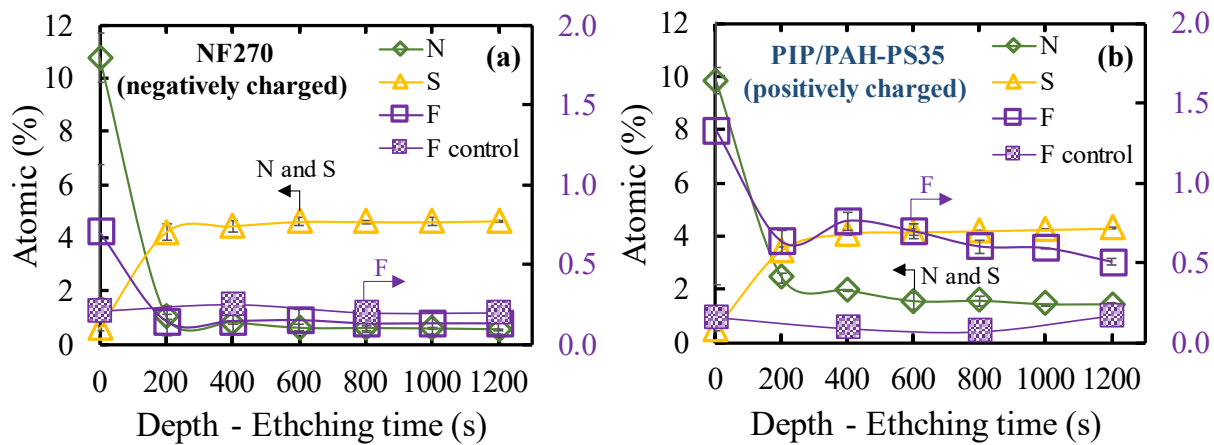


Figure S8. Atomic percentage of fluorine remaining on (a) commercial DOW NF270 and (b) positively charged membranes, after long run filtration and water recovery experiments with a solution containing PFOA (~436 ppm sodium perfluorooctanoate). XPS was run using etching profile. Remaining elemental composition corresponds to C and O.

Membrane characteristics of the PIP-PAH-PS35 are summarized in Table S3.

3.6.3. Analysis of charge effects by using multivalent organic and inorganic anions

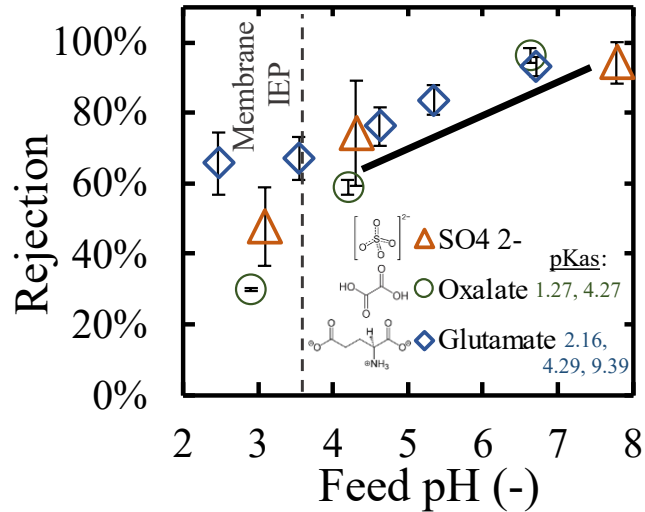


Figure S9. Impact of the surface charge on the separation mechanism. Single solutions of oxalate, glutamate, and sodium sulfate for commercial Dow NF270 membranes. Individual solutions of 1.5-2 mM solute were initially fed. A crossflow membrane system unit was used, with 2-4 membrane cells being tested, $T \sim 25^\circ\text{C}$, $J_w = 65 \pm 15$ (LMH). Oxalate and glutamate were measured through total organic carbon (TOC), and sulfate was calculated from electroneutrality balance. Isoelectric point of the membrane and high-end pH slope is indicated.

Sulfate decrease in rejection as a function of pH as well understood and shown in previous studies for other NF membranes [32].

3.6.4. Kow - octanol-water partitioning coefficient (P):

$$P = \frac{[X]^{org}}{[X]^{aq}} \quad \text{Eq. S4}$$

Where X is the same species in both phases in (mole/volume), aq: octanol-saturated water phase, org: water-saturated octanol phase.

Table S7. Logarithm of the octanol water partitioning coefficient for the linear chain organic compounds tested

Compounds	Log (P (or Kow))
Propionic acid	0.25-0.33 [33]
Pentanoic acid	1.39-1.51 [33]
Octanoic acid	2.93-3.05 [33]
PFOA	4.81-7.75 [8]
PFOS	5.43-7.03 [8]

For fatty acids the bold Log(P) (recommended from source) was used.

For the case of ionizable solutes such as PFOA, PFOS, and the fatty acids tested, the distribution coefficient ((or apparent partitioning coefficient P_{app}) will differ from P (defined only for the same, undissociated, species in both phases) and can be related by the following Equation S4 [33]:

$$P = P_{app} [1 + 10^{(pH-pK_a)}] \quad \text{Eq. S3}$$

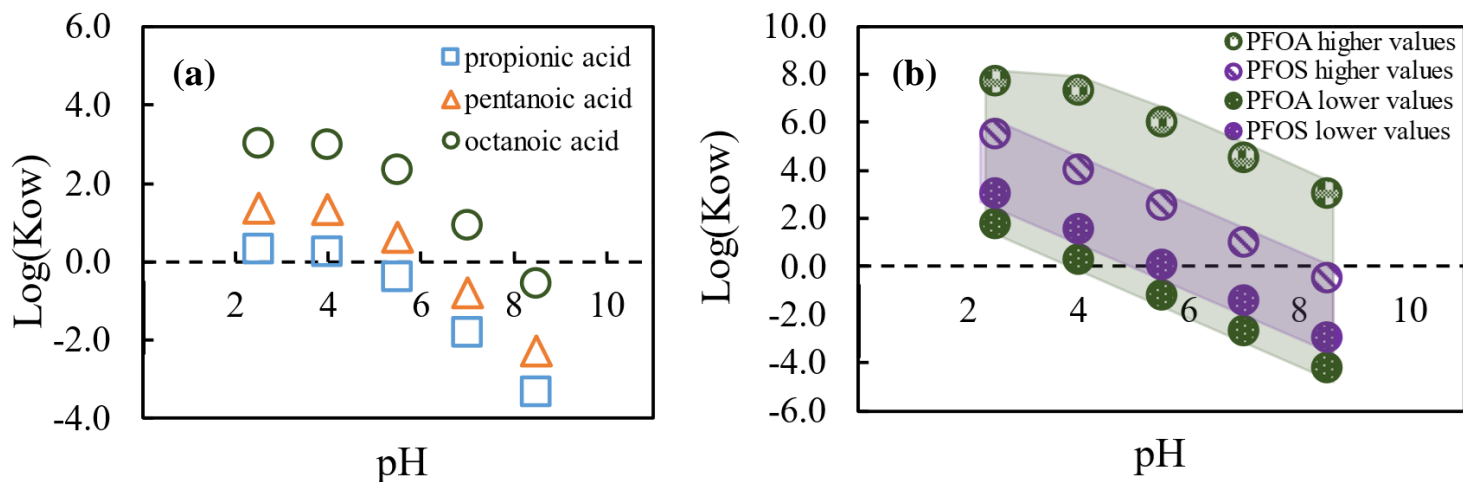


Figure S10. Logarithm of the octanol water partitioning coefficient as a function of pH or Distribution coefficient. (a) Fatty acids (FA), (b) Sensitivity of PFAS due to literature values of pKa and Kow. Values were calculated using Equation S3 at arbitrary pH values.

Analysis of Figure S10:

The tendency for partitioning into the octanol is used to represent the partitioning into the polymeric matrix as both are organic phases, relative to the aqueous phase which is in both the Eq. S4 and the experimental conditions used in our experiments. Therefore, the larger the positive values of the $\text{Log}_{10}(\text{K}_{ow})$ the more the ionogenic compound would like to be in the polymeric (organic) phase. Oppositely, the larger the negative value will represent the ability of partitioning more into the aqueous phase.

As expected at higher pH (>8) these compounds prefer to partition into water (Figure S10), therefore reducing the transport and contributing to an increase in rejection. Shorter chains presented a faster rate of partitioning into the water phase, with a negative value of $\text{Log}(P)$ starting at pH~6. Literature values for K_{ow} (Table S7) and pK_a (Table S1) for PFAS account for a large standard deviation, making this analysis non conclusive.

3.7. Modeling (case scenarios: Na^+ , H^+) against experimental rejections at lowest pH tested:

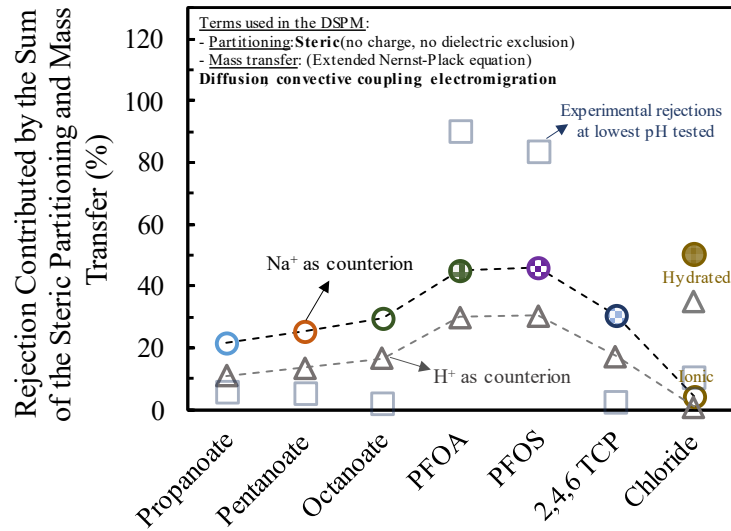


Figure S11. Comparison of the rejection between modeled steric exclusion with H^+ as counterion, Na^+ as counterion, and experimental rejections at the lowest pH tested. Some modeling parameters used were: $X_d=0$, $\epsilon_p = \epsilon_{bulk}$, Na^+ or H^+ as counterion, $J_w=65$ LMH, 0.5 mM of individual solutions, $rp=0.43$ (nm).

The diffusion coefficients at infinity dilution were calculated from limiting molar (equivalent) conductivities as shown below [13]:

$$D_{\infty} = \frac{RT \lambda_0}{F^2 |z|} \quad \text{Eq. S4}$$

Then the Stokes-Einstein equation was used to calculate the radius:

$$r_{s,i} = \frac{kT}{6\pi\eta D_{\infty,i}} * 10^{10} = 0.732 \cdot 10^{-9} \frac{T}{\eta D_{\infty,i}} \text{ (nm)} \quad \text{Eq. S5}$$

Where: T (K), η (g/ cm s), D_{∞} (m/s²)

Table S8. Radii and Diffusion coefficient at infinity dilution of counterion in solutions. Na^+ and H^+ present in evaluated solutions in the body of the manuscript, and Ca^{2+} is included as reference. Calculations were as performed previously [13,21]

Cation	Diffusion coefficient at infinity dilution ($\times 10^{-9} \text{m}^2/\text{s}$), 25°C	Stokes Radii (nm), 25°C
H^+	9.31	0.0264
Na^+	1.335	0.184
Ca^{2+}	0.791	0.310

3.8. Ion balance in the permeate side for selected organic anions solutions

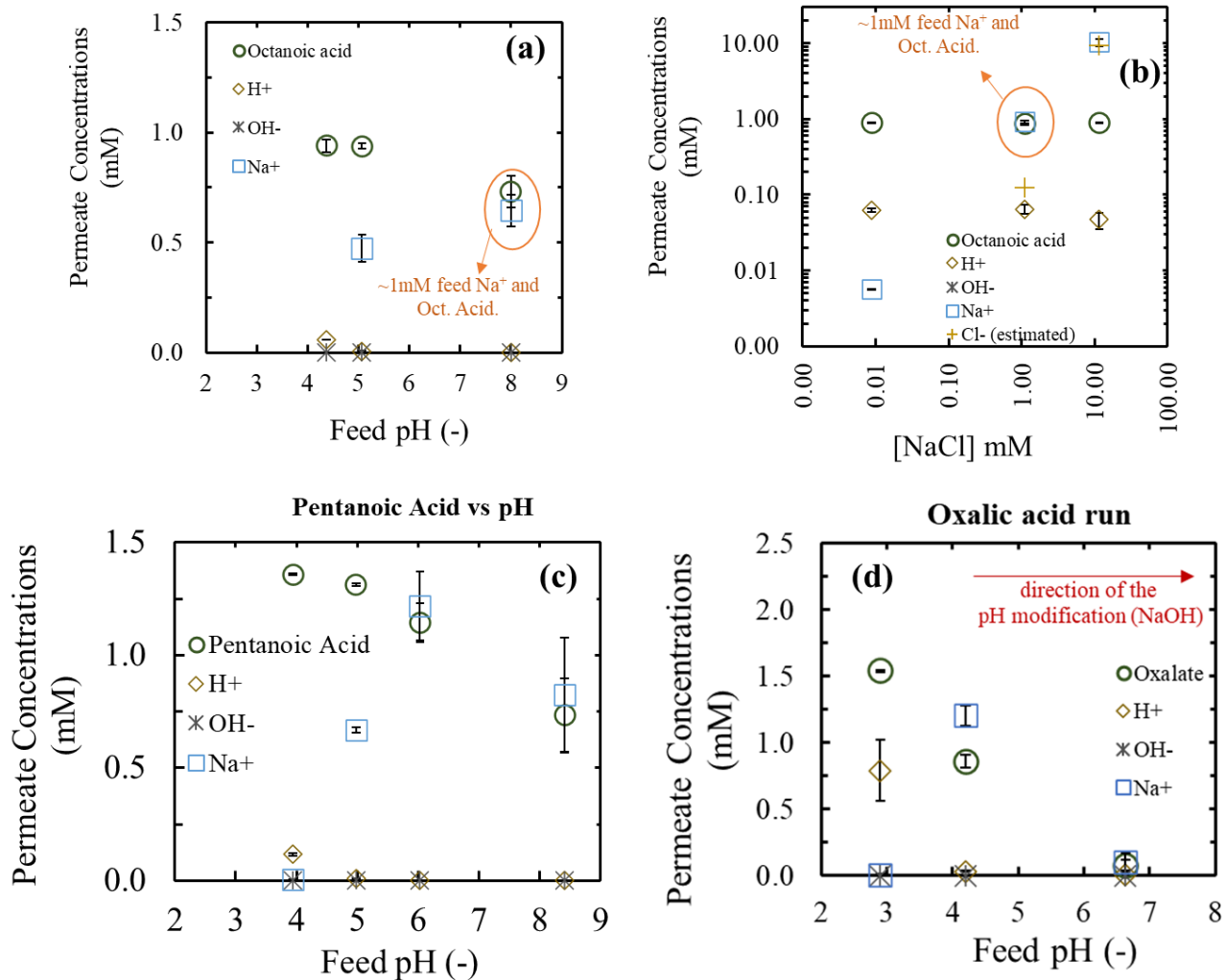


Figure S12. Balance of ions on the permeate samples of some organic anions solutions (a) Octanoic acid vs pH, (b) Octanoic acid vs NaCl concentration, (c) Pentanoic acid. (d) Oxalic acid. Permeate solutions obtained from runs in a cross-flow membrane system, 2-4 membrane were used, $T \sim 26^{\circ}\text{C}$, $J_w \sim 75$ (LMH), 1-2 mM initial feed concentration, and samples were taken after compaction with water and 3 hours of stabilization per measurement. Change in pH was obtained from addition of NaOH. Organic anions were measured through total organic carbon (TOC), Na⁺ were measured through ICP-MS, H⁺ and OH⁻ were calculated from pH measurements.

For the organic anions balance needs to be assess using the pKa values reported in Table S1. At fully ionized conditions ($\text{pH} \gg \text{pKa}$), Na⁺ and organic anion were found to be balanced.

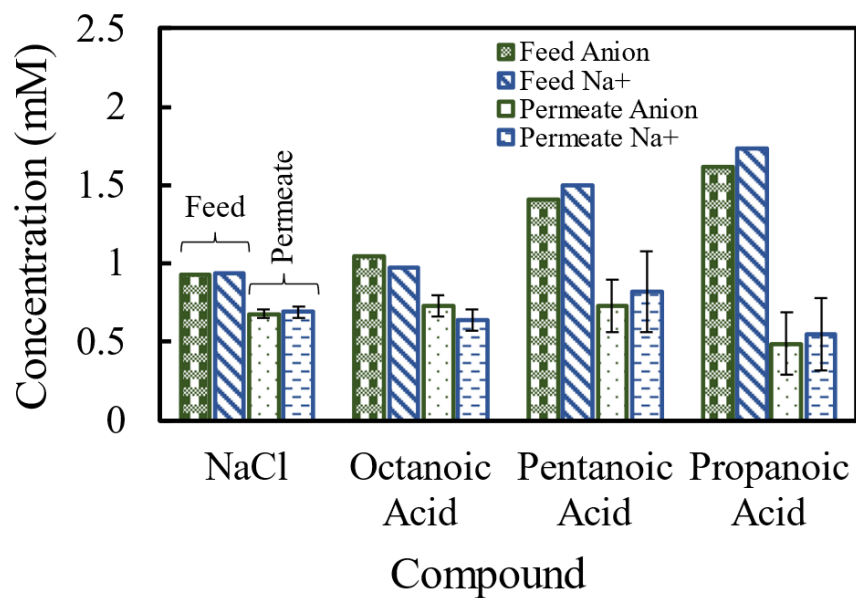


Figure S13. Transport of Na^+ influenced by anion. Comparable feed concentrations of the sodium and organic or inorganic anion yielded a 1:1 passage through the NF membrane. Feed and permeates concentrations correspond to the highest pH tested of the respective anion from Figure 2 in the body of the Manuscript.

3.9. Analysis of counterion as method of detection

ICP-MS analysis for the detection of sodium in Na-PFOA solutions. Comparison of Na⁺ signal linearity against the prepared sample concentration for two different sample vials. EPA recommended centrifuge tubes for PFAS solution showed very good linear correlation between the expected and measured concentrations for solutions as low as 23 ppb sodium. Wide linear range obtained (23-23,000 ppb) is of immense benefit, reducing sample preparation dilutions hassle.

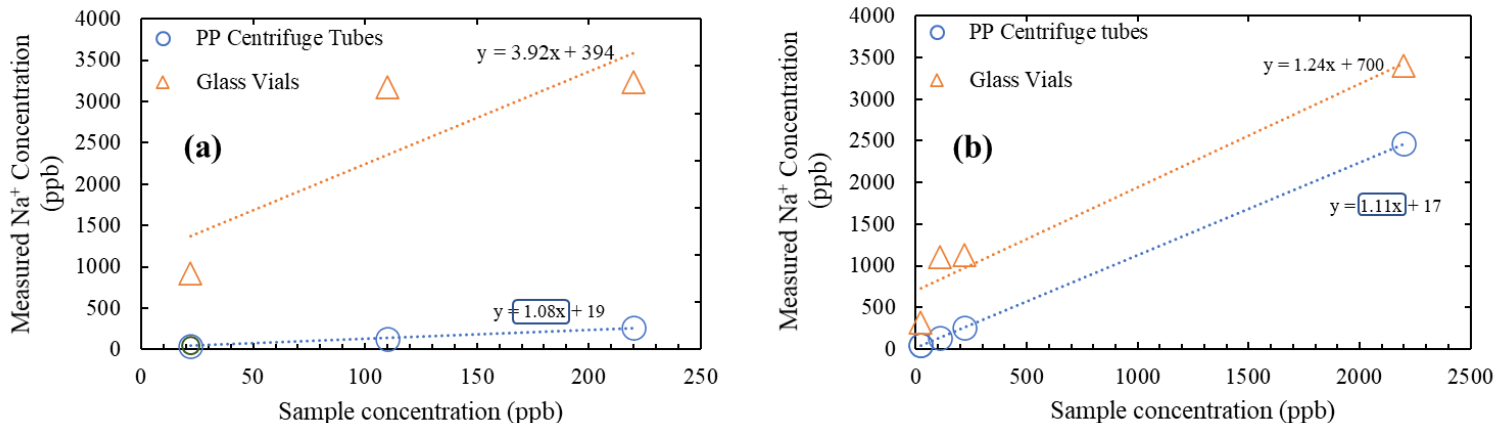


Figure S14. Consistency of perfluorooctanoate measurements by indirect detection of sodium counterion at ppb levels using ICP-MS. (a) 23-230 ppb, (b) 23-23,000 ppb. Impact Also, impact on the detection using proper polypropylene EPA-recommended centrifuge tubes.

4. Characterization of the Thin Polyaromatic Amide Layer on Top of an Open Polymeric Structure

4.1.1. Hydrophilizing effect of pore functionalization of PVDF with hydrogels

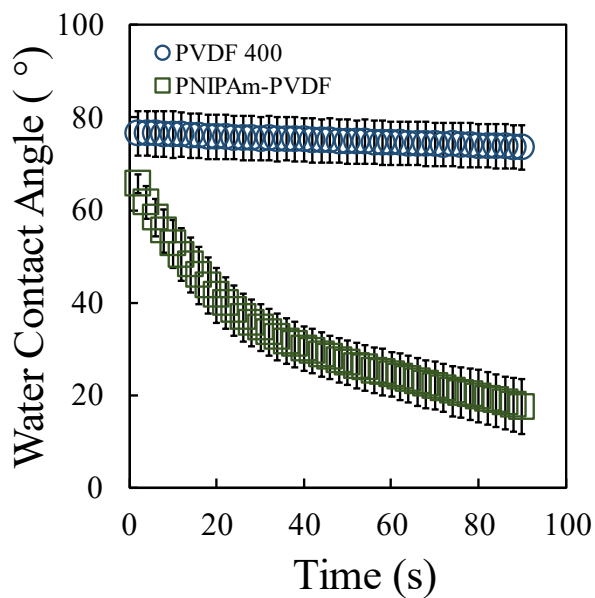


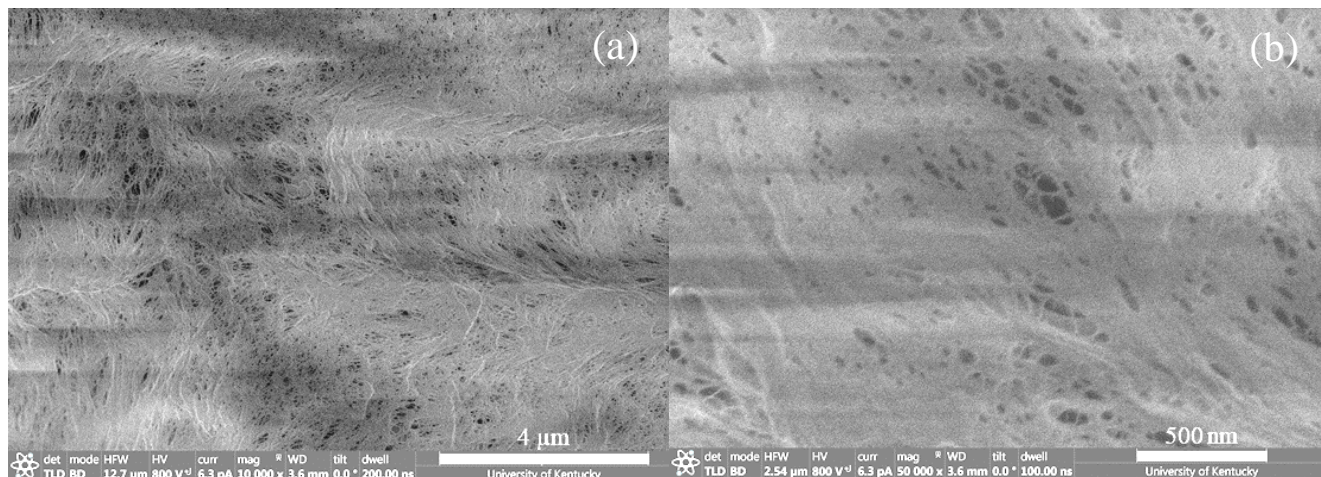
Figure S15. The contact angle of PVDF 400 membranes and PNIPAm-PVDF membranes (weight gain: 14.8%) as a function of time. Error bars represent the standard deviation of 3-5 measurements. The sessile drop method was used to measure contact angle. A time of zero represents the deposition of the drop on the surface.

4.1.2. Scanning electron microscope surface images of bare and functionalized

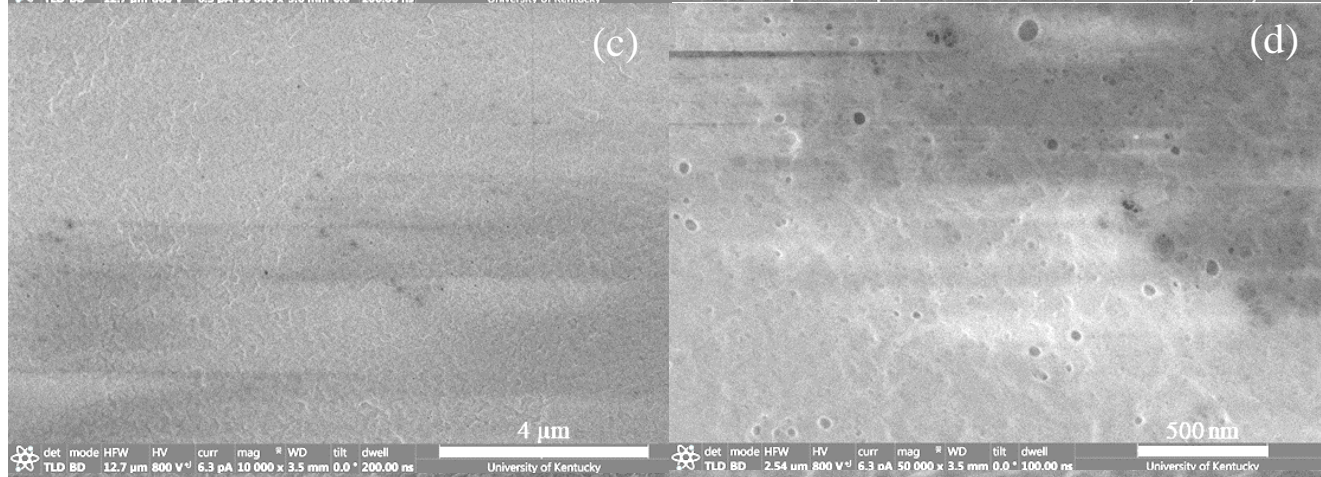
membranes 10,000 x
Magnification

50,000 x
Magnification

PVDF400



PNIPAm-
PVDF



NF-PVDF-
PNIPAm

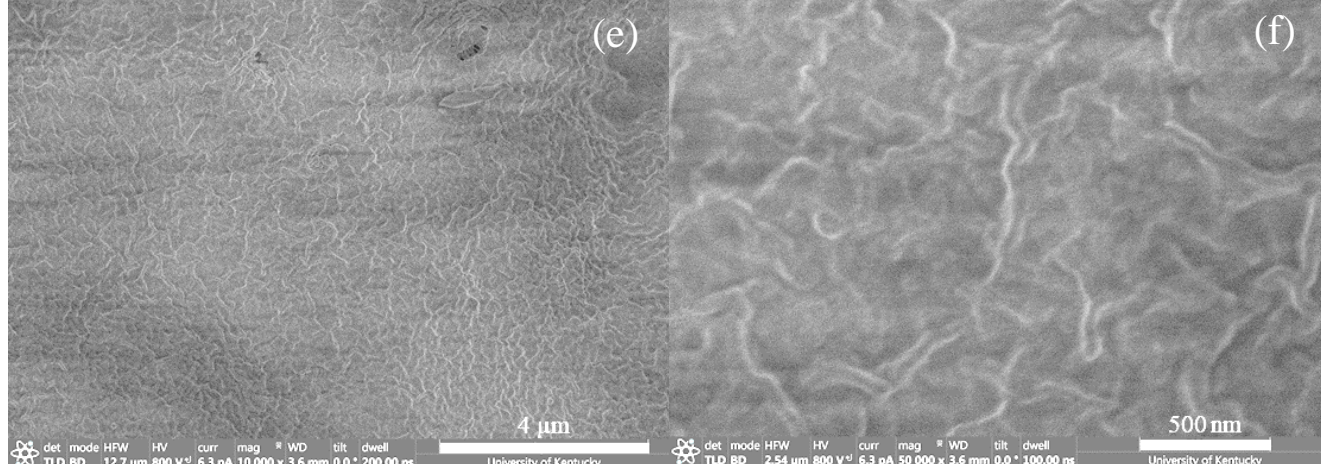


Figure S16. Surface modification from bare PVDF400 (a,b), through pore functionalized PNIPAm-PVDF (c,d) to polyaromatic amide film (e,f). Two magnifications are presented as indicated in figure above. Functionalized materials contain a 10% PNIPAm mass gain.

4.2. Membrane Performance

4.2.1. Separation performance of common organic and inorganic solutes using the synthesized NF-PNIPAm-PVDF:

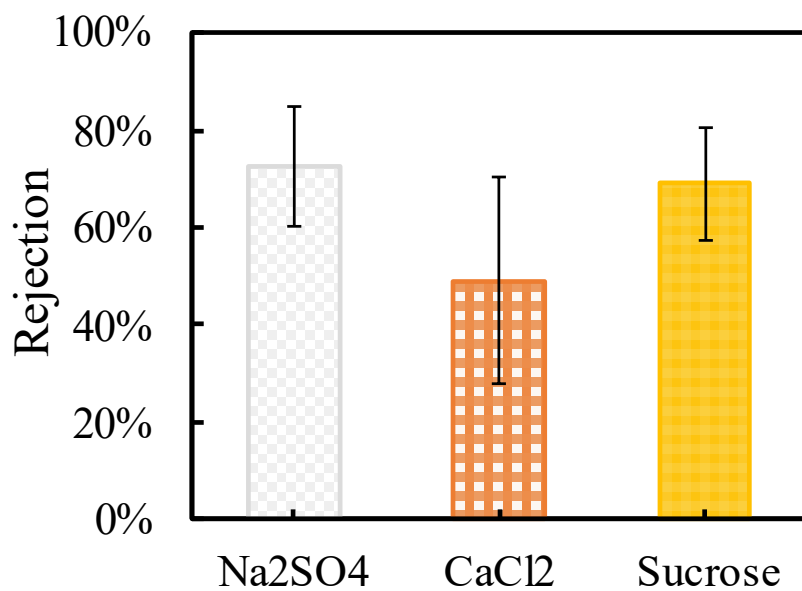


Figure S17. Separation of a neutral organic compound (sucrose 240 ppm) and inorganic salts (Na₂SO₄ 284 ppm and CaCl₂ 111 ppm). Sucrose and Na₂SO₄ were run together in a mix solution (T=27 °C) and CaCl₂ was run as single solution (T=21°C).

4.2.2. Variability between membranes and rejection performance comparison against controls (no interfacial polymerized and commercial NF membranes)

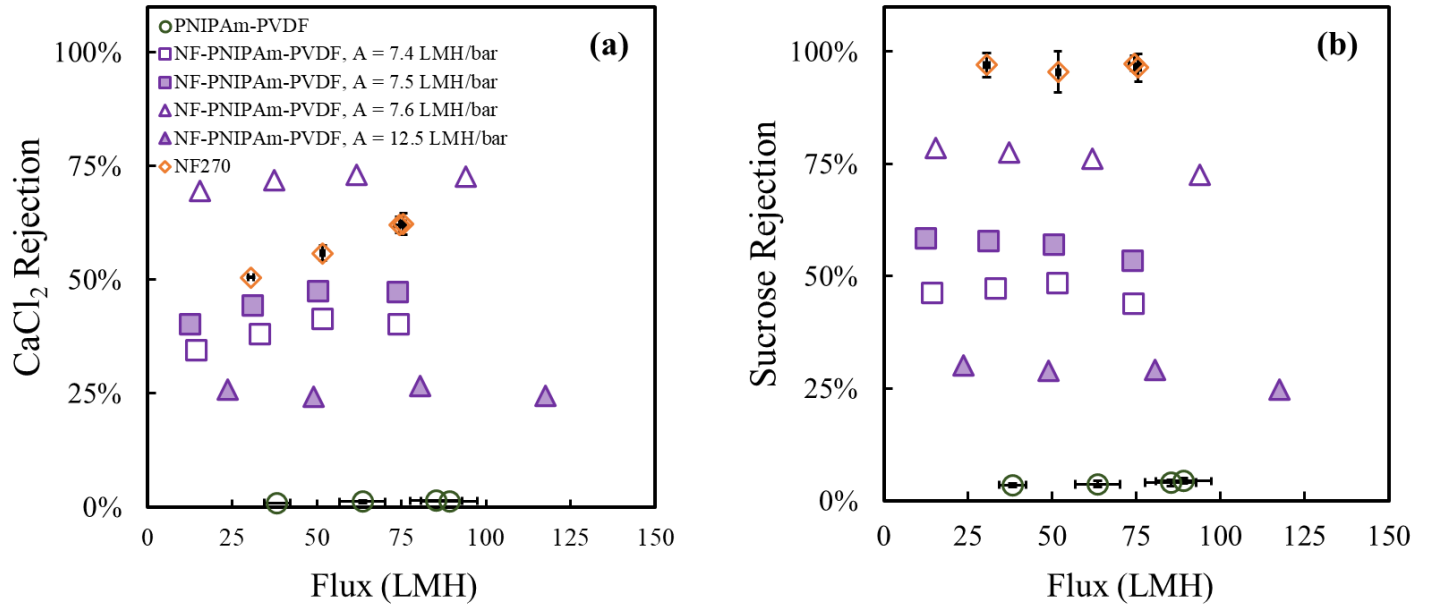


Figure S18 (a) CaCl_2 and (b) sucrose rejections for PNIPAm-PVDF (PNIPAm weight gain of 14.8%), NF-PNIPAm-PVDF (PNIPAm weight gain 10.0% - 11.7%), and NF 270 membranes. A cross-flow unit that maintained the feed at 21°C was used for the measurements. The rejection of both solutes was measured simultaneously with a feed containing ~1 mM of CaCl_2 and ~0.7 mM of sucrose.

4.3. Adsorption experiments

4.3.1. Dynamic adsorption of PFOA on the Synthesized NF-PNIPAm-PVDF membranes

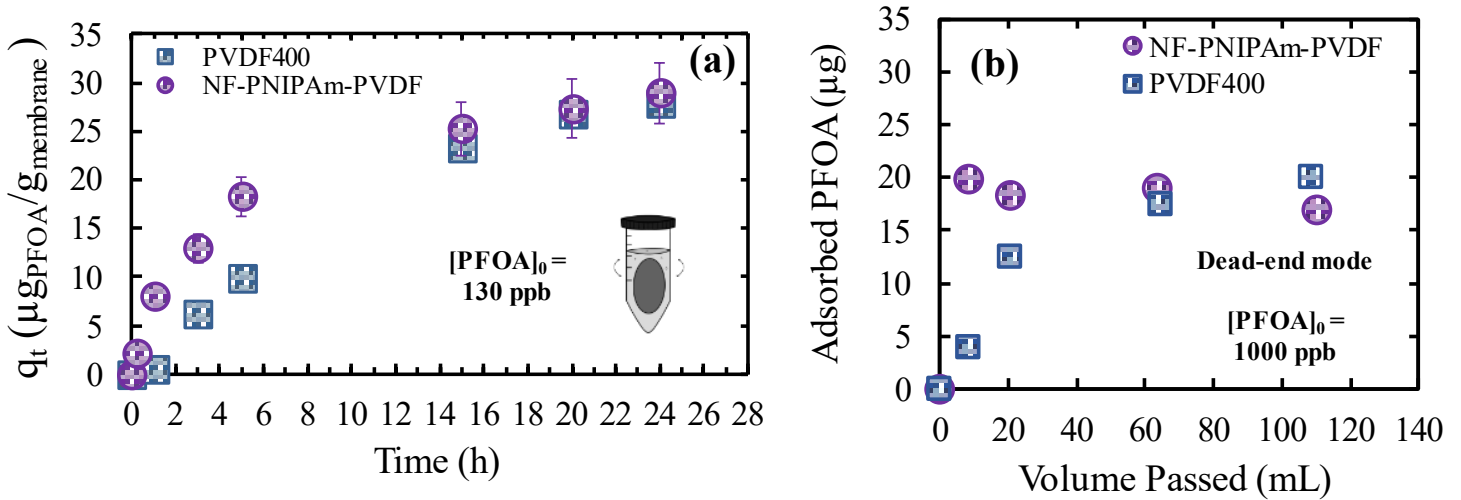


Figure S19. Improved dynamic adsorption. (a) PFOA adsorption over time in a batch mode for the NF-PNIPAm-PVDF membrane and the blank PVDF400. Membranes were set up in a 50 mL centrifuge tube, agitated in a shaking platform at 150 RPM, and temperature kept at 38°C. 48 mL initial volume of a solution with 130 ppb were initially fed. Membranes had 14.6 cm² area, with approximate weights of 0.2 g. The NF-PNIPAm-PVDF membrane contained ~10% PNIPAm. Error bars represent the analytical error from measurements. (b) PFOA adsorption in a dead-end convective flow mode for both NF-PNIPAm-PVDF (PNIPAm mass gain of ~10%; area of 13.2 cm²) and the blank PVDF400. Adsorption steps were conducted by passing ~110 mL (~60% water recovery each time) of 1.0-1.1 ppm PFOA solution through the membrane (14.6 cm² area) at 36-40°C; the pressure was varied from 1.9 to 2.8 bar to achieve a flux of 58-70 LMH. Experiment running time was approximately 34 and 31 min for the total volume passed, for NF-PNIPAm-PVDF and PVDF400, respectively. A stirred (~300 rpm) dead-end cell was used for these measurements.

(a) Calculation of the dynamic adsorption for a batch-diffusive mode at 100 ppb initial concentration of PFOA at 5 hours

$$\text{NF-PNIPAm-PVDF: } \frac{18\mu\text{g}}{300\text{ min}} = 0.06 \left(\frac{\mu\text{g}}{\text{g min}} \right)$$

$$\text{PVDF400: } \frac{10\mu\text{g}}{300\text{ min}} = 0.033 \left(\frac{\mu\text{g}}{\text{g min}} \right)$$

Dynamic adsorption ratio (NF-PNIPAm-PVDF/PVDF400) at 5 hours for a batch diffusive mode:

1.82

(b) Calculation of the dynamic adsorption for dead-end mode at 1 ppm initial concentration of PFOA (Figure S19 (b)) at approximately 6 minutes:

$$\text{NF-PNIPAm-PVDF: } \frac{19.8 \mu\text{g}}{5.93 \text{ min}} = 3.34 (\mu\text{g}/\text{min})$$

$$\text{PVDF400: } \frac{3.97 \mu\text{g}}{5.5 \text{ min}} = 0.72 (\mu\text{g}/\text{min})$$

Dynamic adsorption ratio (NF-PNIPAm-PVDF/PVDF400) at 6 minutes of dead-end flow adsorption: **4.64**

NF-PNIPAm-PVDF seemed to reach its capacity in a dead-end convective flow mode within the first few minutes, in which active sites are more easily available (within the pores). Therefore, in this case, it can be referred as higher dynamic adsorption capacity.

4.3.2. Adsorption selectivity of the PNIPAm functionalized in the NF-PNIPAm-PVDF on

Methylene Blue:

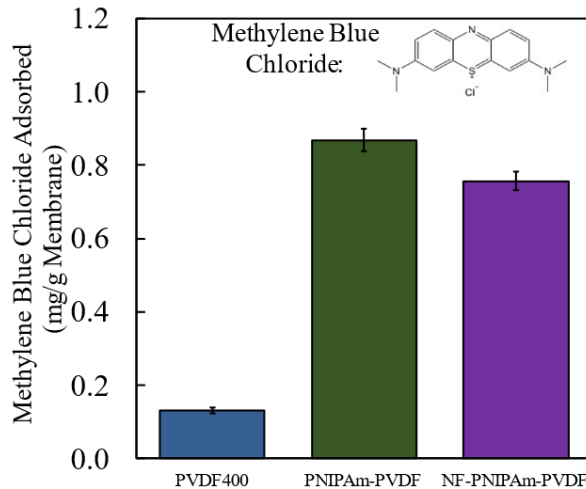


Figure S20. Adsorption capacity of methylene blue by PVDF 400, PNIPAm-PVDF, and NF-PNIPAm-PVDF membranes in a batch mode. Membranes were submerged into methylene blue solutions with an initial concentration of ~4 mg/L and a temperature of ~40°C and shaken at 150 rpm for 24 hours. The PNIPAm-PVDF and NF-PNIPAm-PVDF membranes had a PNIPAm mass gains of 14.8% and 11.7%, respectively.

4.3.3. Desorption of PFOA from NF-PNIPAm-PVDF membranes

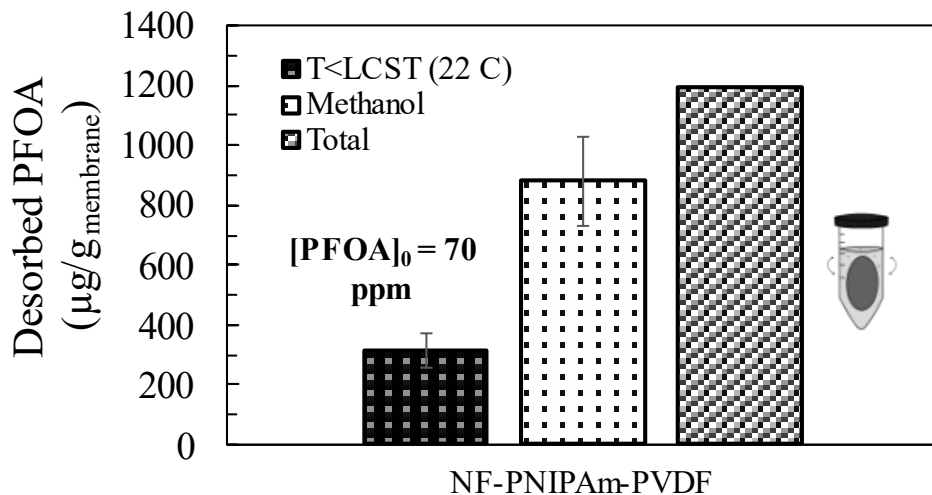


Figure S21. Adsorption capacity and desorption methods. NF-PNIPAm-PVDF membrane were initially used for adsorption of PFOA of an initial solution concentration of 70 ppm for 24 hours. Membrane was taken out from solution, excess solution removed, and the membrane was dried. For the desorption experiment, membrane was placed in a centrifuge tube with 20 mL of water, left in a shaker at 150 RPM, and $T=22 \text{ C}^\circ$. Desorption samples from the solutions were collected at different times, with values within the analytical standard deviation, reporting the average value in the present plot. Afterwards, samples were taken out from the centrifuge tube, excess solution removed, and the membrane was dried, followed by leaving the membrane in a new centrifuge tube with 17 mL of methanol for two days. The solution was then analyzed.

4.4. Experiments under diffusive conditions

4.4.1. Diffusive transport on NF270 and synthesized NF-PNIPAm-PVDF

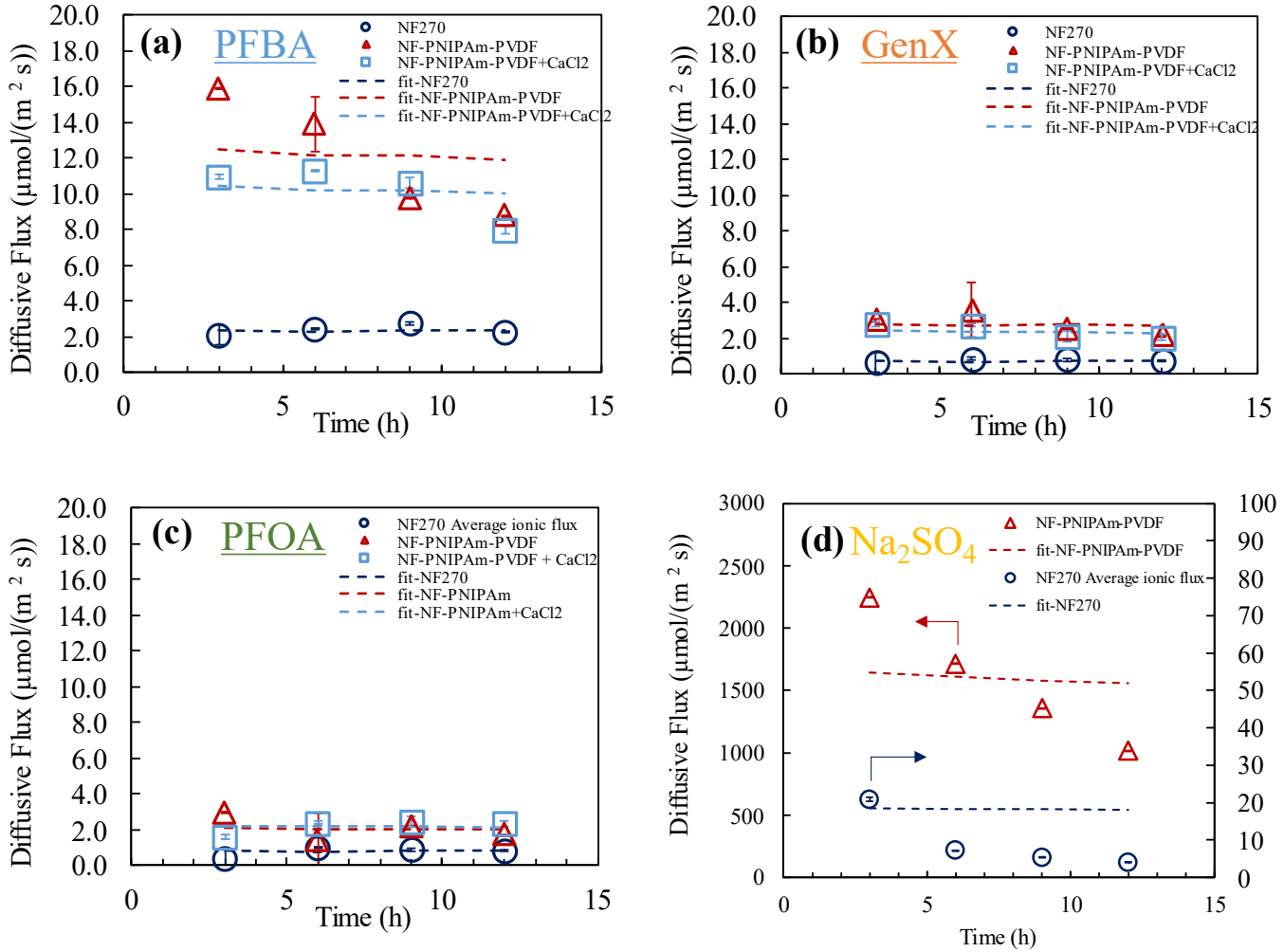


Figure S22. PFAS flux under diffusive condition (no pressure applied using an automated system ILC07 PermeGear) of (a) PFBA, (b) GenX, (c) PFOA, and (d) Na₂SO₄. Two membranes (commercial NF270 and NF-PNIPAm-PVDF) and an extra condition (with addition of 2mM CaCl₂) are presented in plots (a-c). Initial concentration of the PFAS was ~10 ppm each and the experiment was run at 37 °C. For Na₂SO₄ 710 ppm was used as initial concentration, and T=24 C. The fit for a constant feed concentration is presented, from which compounds diffusive permeability coefficient (B) was calculated.

More details about the diffusive instrument and calculations are explained by Aher et. al. [15].

We can talk about an **average** diffusive permeability coefficient since feed concentration may have vary slightly.

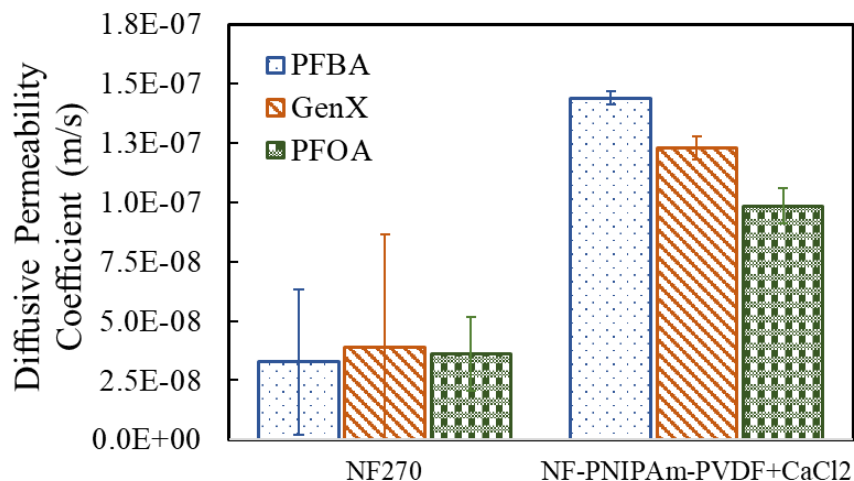


Figure S23. Control runs for diffusive transport of PFAS. Commercial NF270 membrane, and the effect of 2mM CaCl₂ presence in the solution with PFAS. More information about the experiments and from where the diffusive permeability coefficients were calculated can be found in Figure S22.

No CaCl₂ are same results presented in the body of the manuscript to contrast against the case in which 2 mM CaCl₂ is added into the feed solution before starting the diffusive experiment through the synthesized NF-PNIPAm-PVDF. For the case where CaCl₂ was added, both PFBA and GenX B values were lower, indicating a decreased diffusive transport through the NF-PNIPAm-PVDF which is favored by a potential non-covalent bonding occurring between these PFAS and the Ca²⁺ ions.

4.5. Temperature-Responsive Water Permeance

4.5.1. Correcting Water Permeance Values to Account for the Change in the Viscosity of Water

For water permeabilities and water fluxes measured at elevated temperatures, values corresponding to 21°C were computed by correcting for changes in viscosity, as has been done previously by Saad et al. [34]. This adjustment accounts for the changes in water permeability that are caused by changes in the properties of water, thereby giving corrected water permeability values that are indicative of the changes in membrane properties alone (e.g. pore size). While this method was applied to porous PNIPAm-PVDF membranes previously [34], it is also applied to NF-PNIPAm-PVDF and NF270 membranes in this work because both membranes contain a porous support layer and the flow of water through NF membranes has been previously modeled, in a simplified way, as pore flow [35]. The validity of this method for NF membranes was tested using data for NF 270; it was expected that the properties of this membrane would not significantly change with temperature and all increases in water permeability with temperature would be due to changes in the properties of water.

For a porous membrane, the Hagen-Poiseuille equation (Equations S6a) can be applied as an approximation under the assumptions of no-slip at the pore walls and laminar flow inside of uniform and straight pores [34]. The osmotic pressure difference across the membrane was set to 0 bar since the flux tests were conducted using DI water.

$$J_w = \frac{N\pi\Delta P}{8A_m\mu L} \left(\frac{D}{2}\right)^4 \quad (\text{S6a})$$

$$A = \frac{J_w}{\Delta P} = \frac{N\pi}{8A_m\mu L} \left(\frac{D}{2}\right)^4 \quad (\text{S6b})$$

In these equations, J_w is the water flux (LMH), A is the water permeability (LMH/bar), N is the number of pores, ΔP is the pressure difference across the membrane, D is the pore diameter, A_m is the membrane area, μ is the viscosity of water, and L is the membrane thickness. Out of all these variables, the only solvent property was μ . Therefore, J_w and A values that were corrected to 21°C by accounting for changes in μ with temperature were computed using the dependency of J_w and A on μ (see Equations S7a to S7c).

$$J_w \propto \frac{1}{\mu} \quad (\text{S7a})$$

$$J_{w,corrected} = \frac{\mu(T)}{\mu(21^\circ\text{C})} J_w(T) \quad (\text{S7b})$$

$$A_{corrected} = \frac{\mu(T)}{\mu(21^\circ\text{C})} A(T) \quad (\text{S7c})$$

$J_w(T)$, $A(T)$, and $\mu(T)$ are the water flux, water permeability, and viscosity at temperature T ; $\mu(21^\circ\text{C})$ is the viscosity of water at 21°C ($9.82 \cdot 10^{-4}$ Pa s); $J_{w,corrected}$ is the water flux corresponding to the viscosity of water at 21°C; and $A_{corrected}$ is the water permeability corresponding to the viscosity of water at 21°C. After viscosity corrections, the permeability of the NF270 membrane increased only $23\% \pm 1\%$ over the temperature range studied (21°C to 39°C), indicating that this correction method is reasonable for NF membranes.

4.5.2. Impact of the Temperature-Responsive Porous Support on the Water Permeance of the Thin Film Composite (NF-PNIPAm-PVDF)

Model Framework and Calculation Methods

The water permeability of the NF-PNIPAm-PVDF composite membrane was modeled using resistance-in-series and resistance-in-parallel methods to quantify the effect of the support-layer water permeability on the permeability of the composite membrane. This analysis is similar to the one conducted by Werber et al. to calculate the water permeability of composite membranes consisting of a biomimetic selective layer and various types of support layers (e.g. UF, NF, and RO membranes) [36]. This approach assumes that there is no significant lateral flow of water in between the NF layer and the support layer and approximates the support layer as uniform (i.e. negligible lateral variance in transport properties). Any impact that defect edges may have on water permeability was also neglected. A resistance circuit model was used to relate the water-flow resistances to the permeability of the membrane and is shown in Figure S24.

In Figure S24, two paths for water flow are proposed. One path involves in-series water transport through the NF layer and the support layer (labeled 1 in Figure S24) while the other path involves flow through defects in the NF layer (labeled 2 in Figure S24). For flow path 2, the only resistance to water flow is that of the PNIPAm-PVDF support. When considering these two possible paths of

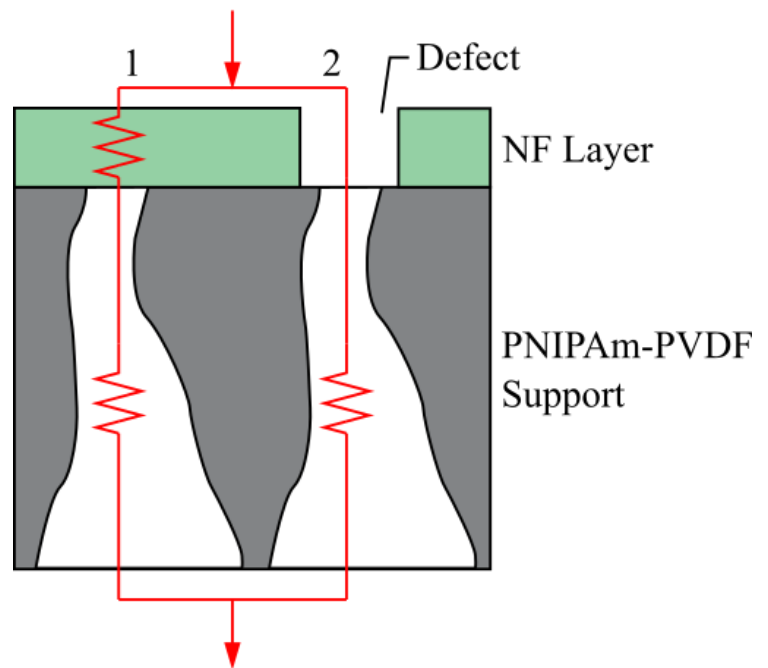


Figure S24. Flow paths and resistances to flow in a NF-PNIPAm-PVDF membrane. Two flow paths are possible: (1) flow through the NF layer followed by the porous support layer and (2) flow through the porous support layer only via defects in the NF layer.

water flow, the measured water permeability of the NF-PNIPAm-PVDF membrane (A) can be expressed using Eq. S8, which sums the permeability contributions of both pathways for water transport.

$$A = A_{Composite}(1 - \theta) + A_{Support}\theta \quad \text{Eq. S8}$$

Here, $A_{Composite}$ is the permeability through the non-defective portions of the membrane, $A_{Support}$ is the permeability of the PNIPAm-PVDF support layer, and θ is the fraction of the membrane surface area where the NF layer is not present (i.e. defective). It should be noted that θ does not encompass additional surface area that would result from any roughness in the NF or UF layers. Using a resistance-in-series model, $A_{Composite}$ can be computed using Eq. S9, where $A_{NF\ Layer}$ represents the water permeability of the selective NF layer alone.

$$\frac{1}{A_{Composite}} = \frac{1}{A_{NF\ Layer}} + \frac{1}{A_{Support}} \quad \text{Eq. S9}$$

It should be noted that viscosity-corrected permeabilities can also be used in Eq. S8 and Eq. S9 because for a given temperature, the same correction factor would be applied to every term in these equations. This analysis used permeabilities that were corrected to 21°C by accounting for changes in water viscosity at elevated temperatures; a similar permeability-correction method was employed in a previous study on PNIPAm-functionalized membranes [34].

To investigate the relationship between the PNIPAm-PVDF support-layer water permeability ($A_{Support}$) and the measured water permeability of the NF-PNIPAm-PVDF membranes (A), the NF layer permeability ($A_{NF\ Layer}$) and the fraction of defects (θ) were estimated using experimental data. Additional values of $A_{NF\ Layer}$ and θ were also considered to assess a variety of possible selective-layer configurations. Then, $A_{Support}$ values were computed at various

temperatures using Eqs. S8 and S9 along with the measured A values for the NF-PNIPAm-PVDF membranes (PNIPAm weight gain of 10.0 -11.7%). The calculated trends for $A_{Support}$ with temperature were then compared to permeability data for PNIPAm-PVDF membranes containing a similar amount of PNIPAm (PNIPAm weight gain of 14.8%) as the NF-PNIPAm-PVDF membranes analyzed in the calculations.

Estimating the Permeability of the NF Layer

Permeability values for the NF layer ($A_{NF\ Layer}$) on the NF-PNIPAm-PVDF membrane were estimated using data collected for other NF membranes. Values for $A_{NF\ Layer}$ at 21°C were estimated by applying Eq. S8 and Eq. S9 to previously collected data from our group on PIP-PS35 membranes [21]. Data for PIP-PS35 membranes was used because the support permeability is known, and the membranes were created using similar methodology compared to the NF-PNIPAm-PVDF membranes. The permeability data presented in this work for N270 (see Figure 6b.1) were used to compute another estimate of the $A_{NF\ Layer}$ at 21°C. For both membranes, the presence of defects was approximated to be negligible ($\theta \sim 0$, $A = A_{Composite}$) due to their high sucrose rejections (> 98%) [21]. Table S9 shows estimates of $A_{NF\ Layer}$ at 21°C for PIP-PS35 and N270 membranes.

Table S9. NF layer permeabilities ($A_{NF\ Layer}$) calculated for PIP-PS35 and N270 membranes at 21°C. Data for PIP-PS35 was reported by Léniz et al [21], and N270 data is presented in Figure 6b.1. $A_{NF\ Layer}$ values were computed using Eq. S8 and Eq. S9 with the assumption of $\theta \sim 0$.

Membrane	Measured Water Permeability, A (LMH/bar)	Measured Support Layer Permeability, $A_{Support}$ (LMH/bar)	Calculated NF Layer Permeability, $A_{NF\ Layer}$ (LMH/bar)
PIP-PS35	9.1	118*	9.9
		50**	25.4
NF270	16.8	200**	18.4
		400**	17.6

*Data collected at 21 °C in a crossflow mode

**A range of permeability values in the UF range was used as an estimation since the support-layer permeability of N270 was unknown

The estimated $A_{NF\ Layer}$ values for 21°C ranged from 9.9-25.4 LMH/bar, so values of 10, 20, and 30 LMH/bar were chosen for modeling.

Data collected for N270 were also used to estimate the dependence of $A_{NF\ Layer}$ on temperature exhibited by NF-PNIPAm-PVDF membranes. First, $A_{NF\ Layer}$ values were computed for N270 at multiple temperatures between 21°C and 39° using Eq. S8 and Eq. S9 with $\theta \sim 0$. The permeability of the support layer was assumed to be constant after viscosity corrections, which would be expected for a porous membrane that lacks temperature-responsive materials. These $A_{NF\ Layer}$ values were lately normalized relative to the $A_{NF\ Layer}$ values for N270 at 21°C. The results of this analysis for N270 membranes are displayed in Figure S25 for multiple estimated $A_{support}$ values.

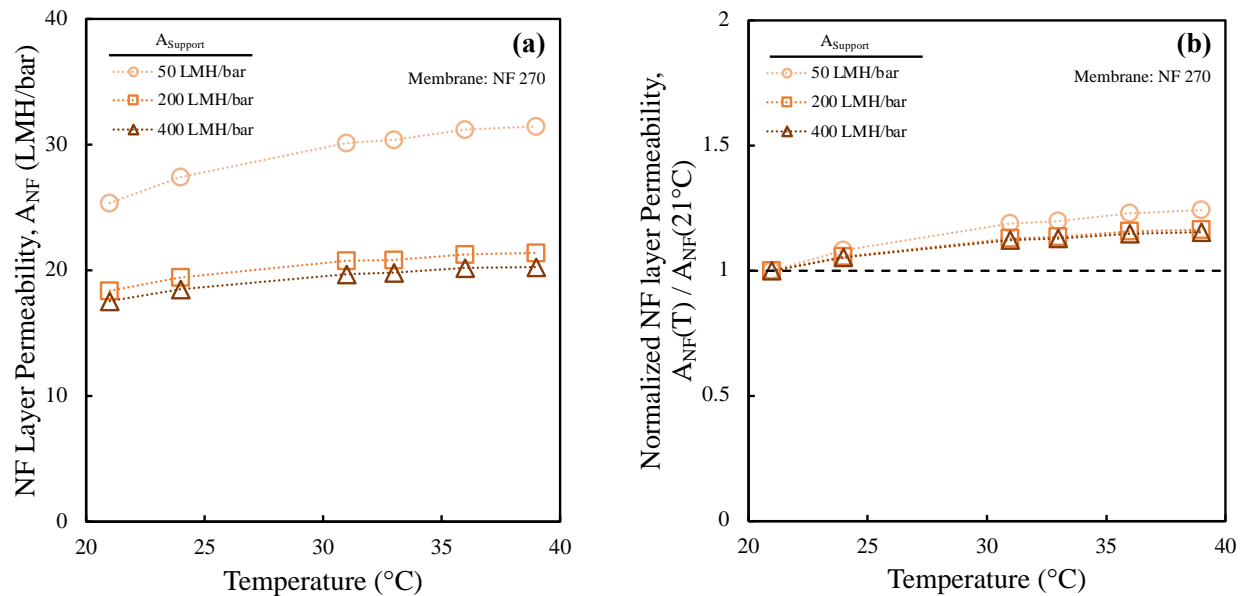


Figure S25. (a) Trends of NF layer water permeability as a function of temperature for NF270 calculated from experimental NF270 permeability data (see Figure 6b.1) and the assumption of minimal defects in the selective layer ($\theta \sim 0$). All permeability values were adjusted to 21°C by correcting for the change in water viscosity with temperature. Support-layer permeability estimates of 50, 200, and 400 LMH/bar were considered. (b) Temperature dependencies of NF layer permeability values after normalization to the NF layer permeabilities calculated at 21°C. Dotted lines were used to signify that plotted data was calculated.

Over the range of $A_{Support}$ values considered, the dependencies of normalized $A_{NF\ Layer}$ values were similar, each steadily increasing from 1 to ~1.2 from 21°C to 39°C. Assuming a similar trend

in NF-layer permeability for the NF-PNIPAm-PVDF membranes, the normalized $A_{NF\ Layer}$ values in Figure S25 (b). along with an estimated $A_{NF\ Layer}$ value at 21°C were used to approximate the relationship between $A_{NF\ Layer}$ and temperature for NF-PNIPAm-PVDF membranes. **Since all the normalized trends of $A_{NF\ Layer}$ were similar for N270, the values corresponding to a support permeability of 200 LMH/bar were used for the analysis on NF-PNIPAm-PVDF membranes.**

Estimating the Fraction of Defects in the NF Layer

SEM images of an NF-PNIPAm-PVDF membrane (see Figures S16e and S16f) were used to approximate the fraction of the surface not covered by the NF layer (θ). While there were no visible defects in image of this membrane at 50,000x magnification, some uncovered pores can be seen in the image at 10,000x magnification. These defects were estimated to cover ~ 0.2% of the imaged membrane area, so a θ value of 0.002 was considered. Higher θ values of 0.01, 0.1, and 0.25 were also considered as it was expected that larger amounts of defects would increase the influence of the support layer on the measured permeability and temperature-permeability relationship for NF-PNIPAm-PVDF membranes.

Computing Required Support Permeabilities for Various NF-Layer Characteristics

For given estimates of θ and $A_{NF\ Layer}$, $A_{Support}$ values corresponding to the experimental permeability trend for NF-PNIPAm-PVDF membranes can be computed. In Figure S26, $A_{Support}$ values for various estimates of θ and $A_{NF\ Layer}$ are shown and compared to experimental values for a PNIPAm-PVDF membrane.

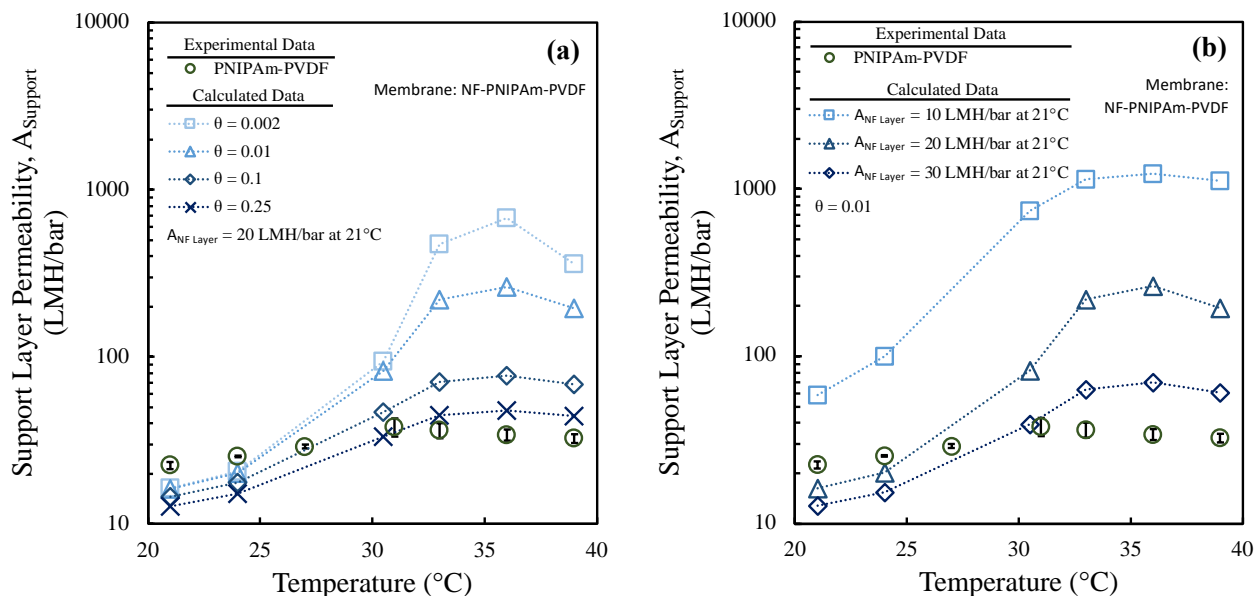


Figure S26. The support-layer water permeability values that correspond to experimental water-permeability data for NF-PNIPAm-PVDF membranes (10.0-11.7% PNIPAm weight gain) in the temperature range of 21°C to 39°C. Support-layer permeabilities were calculated for various (a) defect fractions (θ) and (b) NF layer permeabilities ($A_{NF Layer}$). Experimental data for PNIPAm-PVDF membranes (14.8% PNIPAm weight gain) were also included for comparison. NF-layer permeabilities for NF-PNIPAm-PVDF membranes were assumed to scale with temperature to the same extent as the computed NF-layer permeabilities for N270 (see Figure S23b). All permeability values were adjusted to 21°C by correcting for changes in water viscosity with temperature. Dotted lines were used to signify that plotted data was calculated.

Theoretically, all combinations of θ and $A_{NF Layer}$ had corresponding $A_{Support}$ values that yielded the temperature-responsive permeability that was experimentally observed for NF-PNIPAm-PVDF membranes. However, certain θ and $A_{NF Layer}$ values resulted in calculated $A_{Support}$ values that deviate significantly from experimental permeabilities for PNIPAm-PVDF membranes or are greater than the permeability of the base PVDF 400 membrane (impossible). However, when $A_{NF Layer}$ was fixed, increasing θ led to a lower variance in $A_{Support}$ with temperature that agrees better with experimental PNIPAm-PVDF data. For a fixed θ value of 0.01, increasing $A_{NF Layer}$ yielded $A_{Support}$ values that are closer to the experimental data. These trends in temperature responsivity of $A_{Support}$ versus θ and $A_{NF Layer}$ are also consistent with the relationships in Eq. S8 and Eq. S9. Increasing θ in Eq. S8 heightens the sensitivity of the membrane permeability (A) to changes in $A_{Support}$. Increasing $A_{NF Layer}$ has a similar effect by decreasing the contribution of

$\frac{1}{A_{NF\ Layer}}$ in Eq. S9, thereby increasing the impact of $A_{Support}$ on $A_{Composite}$ and A . In the either case of increasing θ or $A_{NF\ Layer}$, the increased influence of $A_{Support}$ on the A enables temperature-responsivity to be observed for the NF-PNIPAm-PVDF membranes without requiring drastic and unrealistic changes in the $A_{Support}$ with temperature.

Conclusion

Overall, high NF layer permeabilities and a large fraction of defects in the NF layer both increase the impact that the water permeability of the support layer has on membrane permeability. The impact of increasing the NF layer permeability is particularly important in the case where the support permeability and NF layer permeability are similar in value (see Eq. S9). For the NF-PNIPAm-PVDF membrane, the minimal presence of visible defects suggests that the high influence of the temperature responsive nature of the support on the observed water permeability could be driven by a high NF layer permeability that is comparable to the support permeability. This hypothesis is corroborated by the measured permeability of 22.5 ± 1.0 LMH/bar at 21°C for PNIPAm-PVDF membranes with a PNIPAm mass gain of 14.8% (similar to 10.0-11.7% mass gain for NF-PNIPAm-PVDF membranes); this permeability value is within the range of the estimates for the NF-layer permeability in Table S9. Additionally, the low sucrose rejection of the NF-PNIPAm-PVDF membranes compared to N270 membranes (see Figure S18b) suggests the possibility of a loose, highly permeable NF layer within the NF-PNIPAm-PVDF membranes.

- [1] K. Goss, The pKa Values of PFOA and Other Highly Fluorinated Carboxylic Acids, *Environ. Sci. Technol.* 42 (2008) 456–458. <https://doi.org/10.1021/es702192c>.
- [2] B.C. Darcy, D.A. Ellis, H. Li, J.C. McMurdo, E.V.A. Webster, Experimental pKa Determination for Perfluorooctanoic Acid (PFOA) and the Potential Impact of pKa Concentration Dependence on Laboratory-Measured Partitioning Phenomena and Environmental Modeling, *Environ. Sci. Technol.* 42 (2008) 9283–9288. <https://doi.org/10.1021/es802047v>.
- [3] N.O. Brace, Long Chain Alkanoic Acids with Perfluoroalkyl Terminal Segments, *J. Org. Chem.* 27 (1962) 4491–4498.
- [4] J. Cheng, E. Psillakis, M.R. Hoffmann, A.J. Colussi, Acid Dissociation versus Molecular Association of Perfluoroalkyl Oxoacids: Environmental Implications, *J. Chem. PhysicsPhysical Chem. A Lett.* 113 (2009) 8152–8156. <https://doi.org/10.1021/jp9051352>.
- [5] L. Vierke, U. Berger, I.T. Cousins, Estimation of the Acid Dissociation Constant of Perfluoroalkyl Carboxylic Acids through an Experimental Investigation of their Water-to-Air Transport, *Environ. Sci. Technol.* 47 (2013) 11032–11039. <https://doi.org/dx.doi.org/10.1021/es402691z>.
- [6] E. Steinle-Darling, M. Reinhard, Nanofiltration for Trace Organic Contaminant Removal: Structure, Solution, and Membrane Fouling Effects on the Rejection of Perfluorochemicals, *Environ. Sci. Technol.* 42 (2008) 5292–5297. <https://doi.org/10.1021/es703207s>.
- [7] P.N. Breysee, Toxicological Profile for Perfluoroalkyls, 2021.
- [8] F. Xiao, Emerging poly- and perfluoroalkyl substances in the aquatic environment: A

- review of current literature, *Water Res.* 124 (2017) 482–495.
<https://doi.org/10.1016/j.watres.2017.07.024>.
- [9] R.A. Hoke, B.D. Ferrell, T.L. Sloman, R.C. Buck, L.W. Buxton, Aquatic hazard, bioaccumulation and screening risk assessment for ammonium 2, 3, 3, 3-tetrafluoro-2-(heptafluoropropoxy) -propanoate, *Chemosphere.* 149 (2016) 336–342.
<https://doi.org/10.1016/j.chemosphere.2016.01.009>.
- [10] Z.R. Hopkins, M. Sun, J.C. DeWitt, D.R.U. Knappe, Recently detected drinking water contaminants: GenX and other per- and polyfluoroalkyl ether acids, *J. AWWA.* 110 (2018) 13–28. <https://doi.org/10.1002/awwa.1073>.
- [11] A.L. Henne, C.J. Fox, Ionization Constants of Fluorinated Acids, *J. Am. Chem. Soc.* 73 (1951) 2323–2325.
- [12] Y. Moroi, H. Yano, O. Shibata, T. Yonemitsu, Determination of Acidity Constants of Perfluoroalkanoic Acids, *Bull. Chem. Soc. Jpn.* 74 (2001) 667–672.
<https://doi.org/https://doi.org/10.1246/bcsj.74.667>.
- [13] R. R.A, R.H. Stokes, *Electrolyte Solutions, Second Rev*, Butterworth & Co.Ltd, Mineola, New York, 2002.
- [14] D. Mackay, W.-Y. Shiu, S.C. Lee, *Handbook of Physical-Chemical Properties and Environmental Fate for Organic Chemicals*, 2nd ed., CRC Press, 2006.
- [15] A. Aher, T. Nickerson, C. Jordan, F. Thorpe, E. Hatakeyama, L. Ormsbee, M. Majumder, D. Bhattacharyya, Ion and organic transport in Graphene oxide membranes: Model development to difficult water remediation applications, *J. Memb. Sci.* 604 (2020) 118024.

<https://doi.org/10.1016/j.memsci.2020.118024>.

- [16] Y. Roy, M.H. Sharqawy, J.H. Lienhard, Modeling of flat-sheet and spiral-wound nanofiltration configurations and its application in seawater nanofiltration, *J. Memb. Sci.* 493 (2015) 360–372. <https://doi.org/10.1016/j.memsci.2015.06.030>.
- [17] R. Epsztein, E. Shaulsky, N. Dizge, D.M. Warsinger, M. Elimelech, Role of Ionic Charge Density in Donnan Exclusion of Monovalent Anions by Nanofiltration, *Environ. Sci. Technol.* 52 (2018) 4108–4116. <https://doi.org/10.1021/acs.est.7b06400>.
- [18] Y.-L. Lin, Effects of Physicochemical Properties of Nanofiltration Membranes on the Rejection of Small Organic DBP Precursors, *J. Environ. Eng.* 139 (2013) 127–136. [https://doi.org/10.1061/\(ASCE\)EE.1943-7870.0000623](https://doi.org/10.1061/(ASCE)EE.1943-7870.0000623).
- [19] A.J.C. Semião, A.I. Schäfer, Estrogenic micropollutant adsorption dynamics onto nanofiltration membranes, *J. Memb. Sci.* 381 (2011) 132–141. <https://doi.org/10.1016/j.memsci.2011.07.031>.
- [20] D.L. Oatley, L. Llenas, R. Pérez, P.M. Williams, X. Martínez-lladó, M. Rovira, Review of the dielectric properties of nanofiltration membranes and verification of the single oriented layer approximation, *Adv. Colloid Interface Sci.* 173 (2012) 1–11. <https://doi.org/10.1016/j.cis.2012.02.001>.
- [21] F. Léniz-Pizarro, C. Liu, A. Colburn, I.C. Escobar, D. Bhattacharyya, Positively charged nanofiltration membrane synthesis, transport models, and lanthanides separation, *J. Memb. Sci.* 620 (2021). <https://doi.org/10.1016/j.memsci.2020.118973>.
- [22] V. Franke, M. Ullberg, P. McCleaf, M. Walinder, S.J. Kohler, L. Ahrens, The Price of

- Really Clean Water: Combining Nanofiltration with Granular Activated Carbon and Anion Exchange Resins for the Removal of Per- And Polyfluoroalkyl Substances (PFASs) in Drinking Water Production, *Environ. Sci. Technol. Water.* 1 (2021) 782–795. <https://doi.org/https://dx.doi.org/10.1021/acsestwater.0c00141>.
- [23] D. O’Hagan, Understanding organofluorine chemistry. An introduction to the C – F bond, *Chem. Soc. Rev.* (2008) 308–312. <https://doi.org/10.1039/b711844a>.
- [24] Y. Marcus, The Standard Partial Molar Volumes of Ions in Solution. Part 4. Ionic Volumes in Water at 0 - 100 °C, *J. Phys. Chem. B.* 113 (2009) 10285–10291. <https://doi.org/https://doi.org/10.1021/jp9027244>.
- [25] E.R. Nightingale, Jr., Phenomenological theory of ion solvation. Effective radii of hydrated ions, *J. Phys. Chem.* 63 (1959) 1381–1387.
- [26] C.R. Wilke, P. Chang, Correlation of diffusion coefficients in dilute solutions, *AIChE J.* 1 (1955) 264–270. <https://doi.org/10.1002/aic.690010222>.
- [27] W. Schotte, Prediction of the molar volume at the normal boiling point, *Chem. Eng. J.* 48 (1992) 167–172. [https://doi.org/10.1016/0300-9467\(92\)80032-6](https://doi.org/10.1016/0300-9467(92)80032-6).
- [28] J.G. Knudsen, H.C. Hottel, A.F. Sarofim, P.C. Wankat, K.S. Knaebel, Heat and mass transfer: Mass transfer, *CRC Handb. Therm. Eng. Second Ed.* (2017) 417–450. <https://doi.org/10.4324/9781315119717>.
- [29] A.M. Pereira, L.F.G. Martins, J.R. Ascenso, P. Morgado, P.P. Ramalho, E.J.M. Filipe, Diffusion Coefficients of Fluorinated Surfactants in Water: Experimental Results and Prediction by Computer Simulation, *J. Chem. Eng. Data.* 59 (2014) 3151–31–59.

<https://doi.org/dx.doi.org/10.1021/je500211w>.

- [30] M. Li, F. Sun, W. Shang, X. Zhang, W. Dong, Z. Dong, S. Zhao, Removal mechanisms of perfluorinated compounds (PFCs) by nanofiltration: Roles of membrane-contaminant interactions, *Chem. Eng. J.* 406 (2021) 126814. <https://doi.org/10.1016/j.cej.2020.126814>.
- [31] A. Soriano, D. Gorri, A. Urtiaga, Selection of High Flux Membrane for the Effective Removal of Short- Chain Perfluorocarboxylic Acids, *Ind. Eng. Chem. Res.* 58 (2019) 3329–3338. <https://doi.org/10.1021/acs.iecr.8b05506>.
- [32] S. Szoke, G. Patzay, L. Weiser, Characteristics of thin-film nanofiltration membranes at various pH-values, *Desalination.* 151 (2002) 123–129. [https://doi.org/https://doi.org/10.1016/S0011-9164\(02\)00990-6](https://doi.org/https://doi.org/10.1016/S0011-9164(02)00990-6).
- [33] J. Sangster, Octanol-water partitioning coefficients of simple organic compounds, *J. Phys. Chem.* 18 (1989). <https://doi.org/0047-2689/89/031111-120>.
- [34] A. Saad, R. Mills, H. Wan, M.A. Mottaleb, L. Ormsbee, D. Bhattacharyya, Thermo-responsive adsorption-desorption of perfluoroorganics from water using PNIPAm hydrogels and pore functionalized membranes, *J. Memb. Sci.* 599 (2020). <https://doi.org/10.1016/j.memsci.2020.117821>.
- [35] S. Bandini, D. Vezzani, Nanofiltration modeling: The role of dielectric exclusion in membrane characterization, *Chem. Eng. Sci.* 58 (2003) 3303–3326. [https://doi.org/10.1016/S0009-2509\(03\)00212-4](https://doi.org/10.1016/S0009-2509(03)00212-4).
- [36] J.R. Werber, C.J. Porter, M. Elimelech, A Path to Ultraspecificity: Support Layer Properties to Maximize Performance of Biomimetic Desalination Membranes, *Environ. Sci. Technol.*

52 (2018) 10737–10747. <https://doi.org/10.1021/acs.est.8b03426>.